Master's thesis

NTNU
Norwegian University of Science and Technology
Faculty of Medicine and Health Sciences
Department of Clinical and Molecular Medicine

Fredrik Simonsen Frossdal

# Exploring the cGAS-STING axis and DNA damage after infection with respiratory syncytial virus

Master's thesis in Molecular Medicine
Supervisor: Marit Walbye Anthonsen
Co-supervisor: Markus Haug

May 2024

NTNU
Norwegian University of Science and Technology

Fredrik Simonsen Frossdal

# Exploring the cGAS-STING axis and DNA damage after infection with respiratory syncytial virus

Master's thesis in Molecular Medicine
Supervisor: Marit Walbye Anthonsen
Co-supervisor: Markus Haug
May 2024

Norwegian University of Science and Technology
Faculty of Medicine and Health Sciences
Department of Clinical and Molecular Medicine

NTNU
Norwegian University of
Science and Technology

# Acknowledgements

This master's thesis marks the end of my Master of Science in Molecular Medicine at the Norwegian University of Science and Technology. The thesis was conducted at the Department of Clinical and Molecular Medicine (IKOM).

First, I would like to thank my supervisor, Professor Marit W. Anthonsen, for her excellent guidance throughout the year. Your deep knowledge and dedication to the field have been inspiring. I also want to extend my gratitude to Kristin Rian for her invaluable lab training and unwavering determination in finding me a wife. While your attempts may have fallen short, I truly appreciate your heartfelt intentions!

Most of all, I would like to express my gratitude to my fellow students, Elisabeth and Synne. I think writing a master's thesis could be a lonely experience, so I am very grateful that we could work on this together. I had a lot of fun along the way! Lastly, a big thank you to the rest of the class in molecular medicine and the random global health guy, Trevor, for an amazing time at NTNU.

Fredrik Frossdal

May 2024, Trondheim.

# Abstract

Cyclic GMP-AMP synthase (cGAS) is primarily recognized as a cytosolic DNA sensor, activating innate immune responses through the stimulator of interferon genes (STING). However, cGAS has recently been found located in the nucleus of some cell types, where it exhibits a wide range of functions. Additionally, a role for cGAS in the response to certain RNA viruses is just beginning to emerge. In this thesis, we explored the subcellular localization of cGAS during respiratory syncytial virus (RSV) infection in the lung fibroblast cell line, Wi-38. We also investigated genome integrity following RSV infection due to the potential role of self-DNA in cGAS activation.

Our results demonstrated that cGAS was localized predominantly to the nucleus in non-infected Wi-38 cells but translocated to the cytoplasm upon RSV infection. After infection, the expression of the DNA double-strand break marker γH2AX increased. Subsequently, we detected γH2AX, nuclear DNA (nDNA), and mitochondrial DNA (mtDNA) in the cytoplasm of RSV-infected cells. Our results also suggest that nDNA and mtDNA are released extracellularly. However, we detected low overall co-localization between cGAS, the DNA marker DAPI, and γH2AX in the cytoplasm of RSV-infected cells. Furthermore, our results showed a decrease in the expression of lamin A/C and lamin B1 after RSV infection, indicating a weakening of the nuclear envelope. Finally, in a novel model of the post-acute phase of RSV infection, we revealed a continuous increase in γH2AX despite a decline in viral load. We propose a mechanism in which RSV-induced syncytia formation, potentially complimented by reactive oxygen species production, causes cellular damage, leading to disruption of DNA compartmentalization and subsequent cGAS-STING activation.

In summary, this thesis supports a role for the cGAS-STING pathway in response to RSV infection. It highlights the role of cGAS in the detection of self-DNA, providing deeper insights into the mechanisms of innate immunity against RNA viruses.

# Sammendrag

Cyclic GMP-AMP synthase (cGAS) er primært kjent som en cytosolisk DNA-sensor, som aktiverer medfødte immunresponser gjennom stimulator of interferon genes (STING). cGAS har nylig også blitt funnet lokalisert til kjernen i enkelte celletyper, der den utøver et vidt spekter av funksjoner. I tillegg begynner en rolle for cGAS i immunresponsen til enkelte RNA-virus å vise seg. I denne avhandlingen har vi utforsket den subcellulære lokalisering til cGAS i lungefibroblastene, Wi-38, gjennom infeksjon med respiratorisk syncytial-virus (RSV). Vi har også studert genomintegritet etter RSV-infeksjon, på bakgrunn av den mulige rollen til selv-DNA i aktiveringen av cGAS.

Resultatene våre demonstrer at cGAS hovedsakelig var lokalisert til cellekjernen i ikke-infiserte Wi-38 celler, men at den translokerte til cytoplasma etter RSV infeksjon. Etter infeksjon økte ekspresjonen av DNA dobbeltråd brudd markøren γH2AX. Deretter, detekterte vi γH2AX, kjerne-DNA og mitokondrielt-DNA i cytoplasma i RSV-infiserte celler. Resultatene våre antyder også at kjerne-DNA og mitokondrielt-DNA øker ekstracellulær. Imidlertid detekterte vi lav samlokalisering mellom cGAS, DNA markøren DAPI, og γH2AX i cytoplasma i RSV-infiserte celler. Videre, viste resultatene våre synkende ekspresjon av lamin A/C og lamin B1 etter RSV-infeksjon, som indikerer svekkelse av kjernemembranen. Til slutt, i en ny modell for den post-akutte fasen av RSV-infeksjon, viste vi en kontinuerlig økning i ekspresjonen av γH2AX, til tross reduksjon i virusmengde. Vi foreslår en forklaringsmodell der RSV-indusert syncytiadannelse, mulig sammen med produksjon av reaktive oksygenarter, forårsaker DNA lekkasje fra kjerne og mitokondrie, som til slutt fører til cGAS-STING aktivering.

Oppsummert, denne avhandlingen underbygger en rolle for cGAS-STING signalveien i responsen til RSV infeksjon. Den fremhever cGAS rolle i deteksjon av selv-DNA, og gir dypere innsikt i den medfødte immunresponsen mot RNA-virus.

# Content

# Abbreviations

| | |
|---|---|
| ALR | AIM-2-like receptor |
| cGAMP | 2’3’-cyclic GMP-AMP |
| cGAS | 2’3’-cyclic GMP-AMP synthase |
| CLR | C-type lectin receptors |
| COPD | Chronic obstructive pulmonary disease |
| DAMP | Damage associated molecular pattern |
| DAPI | 4′,6-diamidino-2-phenylindole |
| DNA | Deoxyribonucleic acid |
| DSB | Double stranded breaks |
| eIF2α | Eukaryotic initiation factor 2α |
| ER | Endoplasmic reticulum |
| FFU/mL | focus forming units per milliliter |
| GAPDH | Glyceraldehyde 3-Phosphate Dehydrogenase |
| GFP | Green fluorescent protein |
| IFN | Interferon |
| IFNAR | Interferon-α/β receptor |
| IRF3 | Interferon regulatory factor 3 |
| ISG | Interferon stimulated genes |
| ISRE | IFN-stimulated response element |
| JAK-STAT | Janus kinase-signal transducer and activator of transcription |
| LRTI | Lower respiratory tract infection |
| MAVS | Mitochondrial antiviral-signaling protein |
| MOI | Multiplicity of infection |
| mtDNA | Mitochondrial DNA |
| nDNA | Nuclear DNA |
| NF-κB | Nuclear factor kappa-light-chain-enhancer of activated B cells |
| NLR | Nod-like receptor |
| PAMP | Pathogen associated molecular pattern |
| PERK | PKR-like endoplasmic reticulum kinase |
| PRR | Pattern recognition receptor |
| RdRp | RNA-dependent RNA polymerase |

| | |
|---|---|
| rgRSV | Recombinant green fluorescent protein-expressing respiratory syncytial virus |
| RLR | RIG-I-like receptor |
| RNA | Ribonucleic acid |
| RSV | Respiratory syncytial virus |
| RTI | Respiratory tract infection |
| SARS-CoV-2 | Severe acute respiratory syndrome coronavirus 2 |
| SASP | Senescence associated secretory phenotype |
| SAVI | STING-associated vasculopathy with onset in infancy |
| STAT1 | Signal transducer and activator of transcription 1 |
| STING | Stimulator of interferon genes |
| TBK1 | TANK-binding kinase 1 |
| TLR | Toll-like receptor |
| URTI | Upper respiratory tract infection |
| γH2AX | Phosphorylated form of histone 2A family member X (Ser139) |

# 1. Introduction

## 1.1 Viral respiratory tract infections

Respiratory tract infections (RTIs) are the most frequent illnesses to humans, and the majority of RTIs are caused by viral infections (1). RTIs represent a significant cause of mortality among children under the age of five, particularly in developing countries, where they manifest with higher frequency and severity (1, 2). Additionally, mainly due to the high attack rate, viral RTIs impose a greater economic burden than many other clinical conditions including asthma, migraine, and congestive heart failure, highlighting the need for increased knowledge and management of RTIs (3).

RTIs can manifest as upper respiratory tract infections (URTI), lower respiratory tract infections (LRTI), or both. URTIs are infections of the mouth, nose, throat, larynx, and trachea, and are in most cases of viral origin, resulting in uncomplicated spontaneous resolution (4, 5). However, especially in infants, viral URTIs can in some cases progress to LRTIs characterized by more pronounced symptoms like wheezing, severe coughing, breathlessness, and respiratory distress, which might pose a significant risk to the patient. LRTIs includes conditions such as bronchitis, bronchiolitis and pneumonia, which tend to be more severe than URTIs (6).

Adenovirus, influenza viruses, parainfluenza viruses, rhinovirus, and respiratory syncytial virus (RSV), are historically the viruses most frequently involved in URTIs (1, 4). While much attention has been diverted to severe acute respiratory syndrome coronavirus 2 (SARS-CoV-2) since its global outbreak in early 2020, RSV is particularly harmful to infants (7, 8). Therefore, this thesis will be focused on RSV.

RSV was first isolated from infants suffering from LRTIs back in 1957 and has since then been one of the leading causative agents of RTIs, known to infect virtually all children before the age of two (9, 10). While RSV infection typically presents as URTIs, it was estimated that RSV caused more than 33 million cases of severe acute LRTIs in 2015, leading to 3.2 million hospitalizations and about 60.000 in-hospital deaths in children under the age of five globally. The overall mortality was estimated to be as high as 120.000 annually, accounting for children with limited access to healthcare (11).

Reinfections are frequent occurrences in adults, persisting throughout their lives. Additionally, individuals with underlying health conditions and the elderly face an elevated risk of experiencing severe complications, leading to morbidity and mortality rates comparable to that

of non-pandemic influenza viruses (12). Patients suffering from chronic obstructive pulmonary disease (COPD) may be especially vulnerable and can experience severe exacerbations upon infection (13). Moreover, RSV infection is also suspected to play a role in the long-term development of asthma, and some patients experience lasting respiratory issues, like wheezing, after infection (14). Additionally, severe RSV infection can be involved in the long-term development of pulmonary fibrosis, which impair lung function (15). Recently, the first RSV vaccines for the elderly (≥ 60 years of age) were approved, but currently, the only form of preventative treatment for infants is based on the administration of monoclonal antibodies (16, 17). Thus, there is still an urgent need for new research on RSV-mediated immune mechanisms.

## 1.2 Structure and function of the respiratory syncytial virus virion and proteins

RSV is a non-segmented, enveloped, negative-sense, single-strand RNA virus of the Paramyxoviridae family and Pneumovirus genus (18). The RSV genome encodes 11 proteins transcribed from 10 genes. The mature virion displays the attachment glycoprotein (G), the fusion glycoprotein (F), and the small hydrophobic protein (SH) on the lipid bilayer surrounding the nucleocapsid (19) (Fig. 1a). The envelope is further supported by the matrix proteins M and M2-1, with the latter also working as a transcription processivity factor. In addition, the M2-1 protein mediates the interaction with the ribonucleoprotein complex (RNP), which consists of viral RNA and the nucleoprotein (N). The large polymerase subunit (L), a phosphoprotein polymerase co-factor (P), and N make up the RNA-dependent RNA polymerase complex (RdRp), which is also connected to the RNP in the mature virion (Fig. 1a) (20). Shortly after entry, the non-structural proteins NS1 and NS2 are transcribed, which inhibit apoptosis and interferon (IFN) induction and signaling (21). M2-2 has overlapping open reading frames with M2-1, and is transcribed after ribosomal reinitiation late in infection, which governs a switch from protein synthesis to genome replication (Fig. 1b) (22).

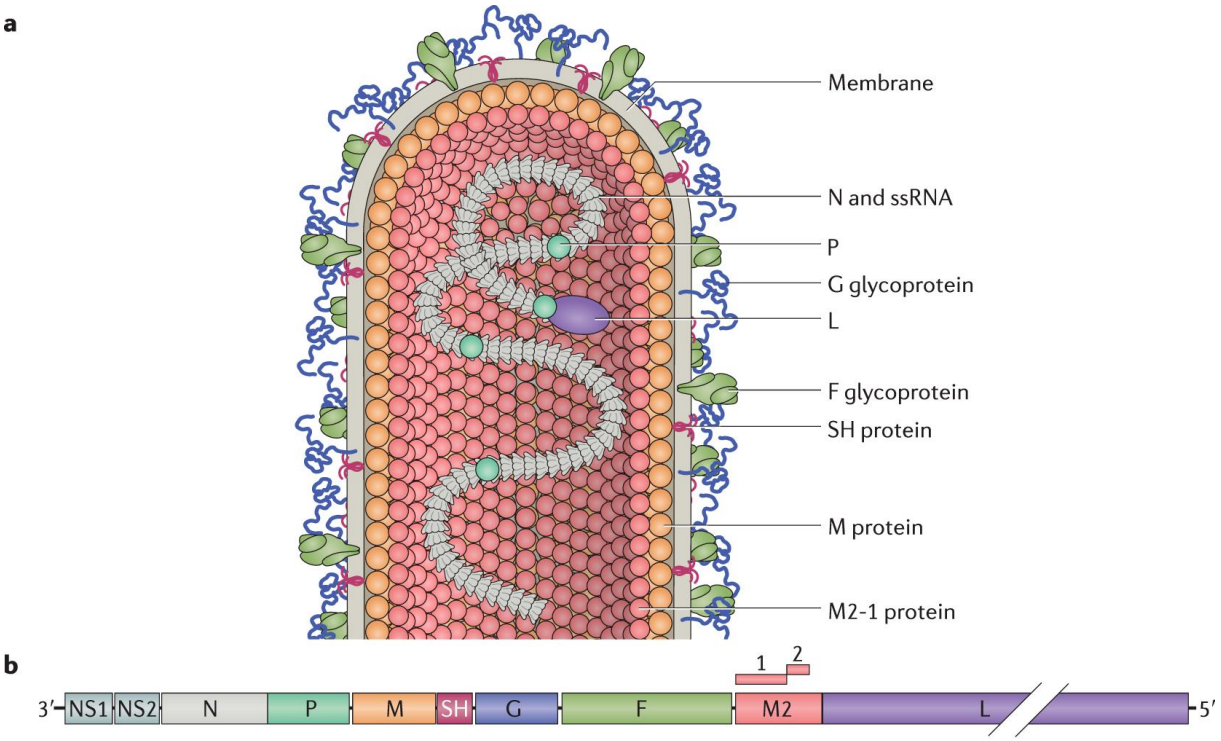


**Figure 1: The structure of the mature RSV virion. (a).** The ribonucleoprotein complex (RNP) consists of the RSV genome and the nucleoprotein (N). In addition, the RNA-dependent RNA polymerase complex (RdRp), consisting of the large polymerase subunit (L), a phosphoprotein polymerase co-factor (P), and N, is bound to the RNP. The RNP is bound to the matrix 2-1 (M2-1) protein, which mediates the interaction with the matrix protein (M). Together, they support the envelope, in which the attachment glycoprotein (G), the fusion glycoprotein (F), and the small hydrophobic protein (SH) are inserted, the latter being an ion channel. **(b).** The negative-sense single-stranded RSV genome contains 10 genes encoding 11 proteins. In addition to the protein mentioned in **a,** the non-structural proteins NS1 and NS2 are transcribed upon entry, and the matrix 2-2 protein (M2-2) is transcribed late in infection upon ribosomal reinitiation. Figure adapted from (20).

Ciliated bronchial epithelial cells are the primary target for RSV infection (23). Although the details of RSV entry are poorly understood, the viral G-protein is thought to use heparan sulfate (HS) as the main attachment point on ciliated cells in the respiratory tract (20). However, non-ciliated cells such as lung fibroblasts are also commonly infected with RSV, and are shown to participate in the antiviral response (24). Moreover, lung fibroblasts, like the Wi-38 cells used in this thesis, express HS on their cell surface and likely contribute to viral entry (24). In addition, the widely expressed protein nucleolin, has been shown to drive infection through its interaction with the viral F-protein, revealing another way of attachment to the target cell (25, 26). Even though the F protein is involved in attachment, it is primarily recognized for its role in facilitating entry (19). The F protein inserts its hydrophobic residues into the membrane of the target cell, before refolding and dragging the viral envelope close to the cell membrane,

leading to fusion (19). The F protein is synthesized as a large precursor protein called $F_0$, which is post-translationally cleaved by host proteases during viral maturation, yielding the smaller $F_1$ and $F_2$ subunits. The $F_1$ and $F_2$ proteins are covalently linked through two disulfide bonds and are fusion-competent upon trimer formation (20).

One of the most notable features of RSV is the tendency of infected cells to form large multinucleated cells called syncytia. Syncytia form when the viral F-protein is expressed on the membrane of infected cells, binding to adjacent cells and causing fusion, thereby enabling direct cell-to-cell transmission. (27). Syncytia formation leads to lesions in the epithelial cell lining of the airways, which contribute to the symptoms associated with infection (27-29).

## 1.3 Innate immune response against respiratory viruses

An important aspect of the innate immune system is the cells' ability to distinguish between pathogenic and non-pathogenic entities and induce an appropriate response. For this, cells have pattern recognition receptors (PRRs), capable of responding to a broad range of pathogen-associated molecular patterns (PAMPs) and damage-associated molecular patterns (DAMPs) (30). There are many types of PRRs, including Toll-like receptors (TLRs), Nod-like receptors (NLRs), C-type lectin receptors (CLRs), and various intracellular nucleic acid receptors such as 2'3'-cyclic GMP-AMP (cGAMP) synthase (cGAS), AIM2-like receptors (ALRs), and RIG-I-like receptors (RLRs), with the former two sensing DNA in the cytosol and the latter foreign RNA (30-32).

PRRs trigger a range of signaling cascades and subsequent gene regulation, which tune the innate and adaptive immune response specifically to the pathogen detected (30). IFNs are among the genes upregulated downstream of certain PRRs and are especially important for an antiviral response (33). There are three types of IFNs, each activating distinct heterodimeric receptors. These receptors signal through the Janus kinase-signal transducer and activator of transcription (JAK-STAT) pathway, thereby activating the transcription of IFN-stimulated genes (ISGs) (Fig. 2) (33). Many ISGs with distinct functions exist, but a common feature is their role in resisting and controlling pathogens (34).

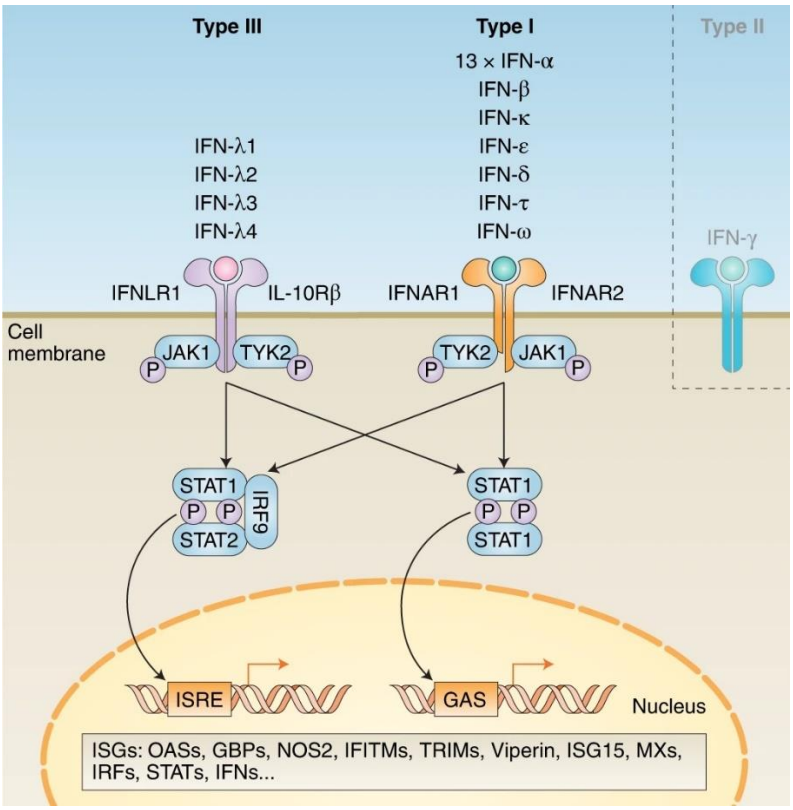


**Figure 2: Overview of the three classes of IFNs, their receptors, and downstream signaling events**. Adapted from (33).

Although some viral-encoded products can be detected by PRRs, recognition of foreign nucleic acid is the predominant method of viral detection and is essential for rapid clearance (35). RNA-viruses, like RSV, are generally recognized by cytoplasmic RNA-sensors such as RLRs or the endosomal RNA-sensors like TLR 3, 7 and 8 (36-38). However, viruses have evolved evasion strategies to circumvent the initial immunodetection, illustrated by the low to undetectable levels of type I IFN associated with RSV infection (39). In fact, the NS1 and NS2 proteins encoded by RSV, are known to directly interfere with the central RLRs, RIG-I and MDA5, and their downstream adaptor, mitochondrial antiviral-signaling protein (MAVS). Additionally, NS1 and NS2 interfere with JAK/STAT signaling, thereby efficiently hindering both the interferon production and the induction of ISGs (39). Thus, due to effective immune evasion of RSV and other viruses, cells need diverse methods to detect and combat viral infection.

## 1.4 The canonical cGAS-STING pathway.

cGAS is a PRR known for its role in sensing host or microbial double-stranded DNA in the cytosol. Upon DNA binding, cGAS synthesizes the cyclic dinucleotide cGAMP, which subsequently binds stimulator of IFN genes (STING), localized to the cytosolic side of the endoplasmic reticulum (ER) membrane (32). STING then undergoes a conformational change, leading to dimerization and translocation through the trans-Golgi network. Here, STING is phosphorylated and bound by TANK-binding kinase 1 (TBK1), which undergoes transautophosphorylation. Interferon regulatory factor 3 (IRF3) is recruited to the phosphorylated site of STING and is also phosphorylated by TBK1. Phosphorylated IRF3 then dimerizes and translocates to the nucleus, where it activates the transcription of type I IFNs (32). Type I interferons are secreted into the extracellular space, where they bind to the IFNα/β receptor (IFNAR). IFNAR engagement initiates signaling through the JAK-STAT pathway, leading to the induction of ISGs and a potent antiviral response. (40) (Fig. 3).

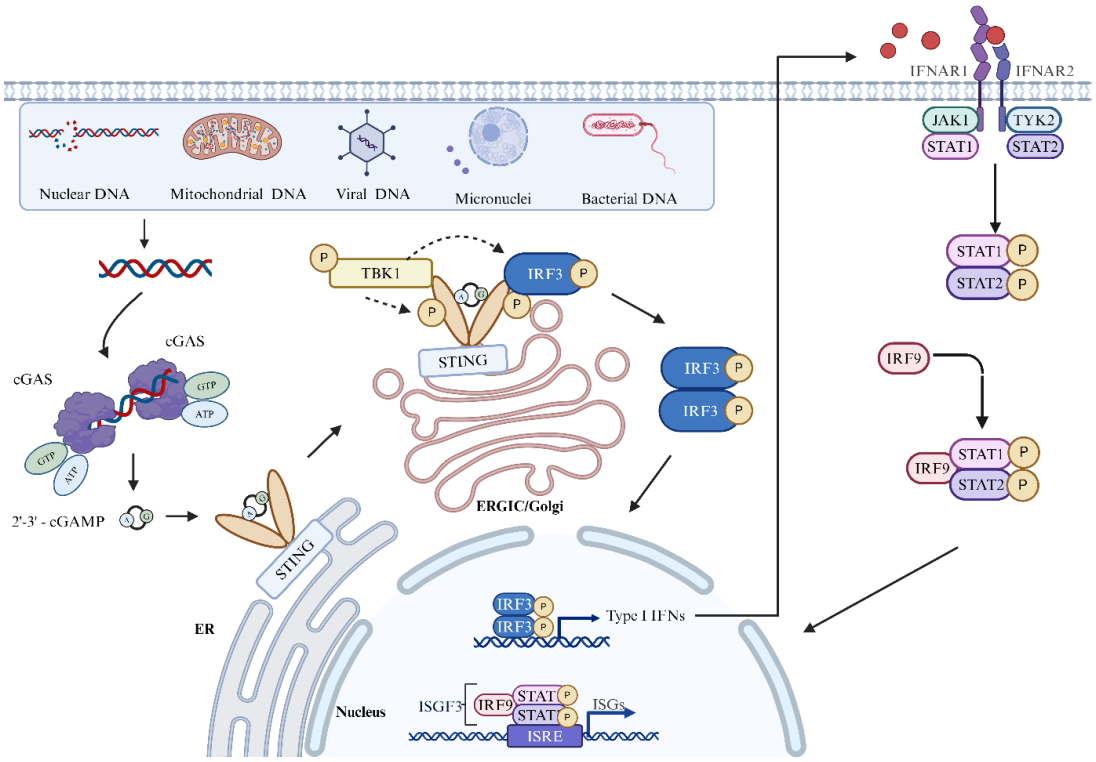


**Figure 3: The canonical cGAS-STING pathway.** DNA enters the cytoplasm and is bound by cyclic GMP-AMP (cGAMP) synthase (cGAS), which produces the cyclic dinucleotide cGAMP. cCAMP binds to stimulator of interferon (IFN) genes (STING). STING undergoes a conformational change and translocates from the endoplasmic reticulum (ER) to the Golgi through the ER-Golgi intermediate compartment (ERGIC). Here, TANK-binding kinase 1 (TBK1) binds STING and phosphorylates STING itself and the interferon regulatory factor 3 (IRF3). Phosphorylated IRF3 forms homodimers and translocates to the nucleus, where it activates transcription of type I IFNs. IFNs are secreted, where they can bind the heterodimeric transmembrane receptor called the IFNα

receptor (IFNAR), consisting of IFNAR 1 and 2. The receptor activates Janus kinase 1 (JAK1) and tyrosine kinase 2 (TYK2), which phosphorylate the signal transducer and activator of transcriptions 1 and 2 (STAT 1 and 2). STAT 1 and 2 dimerize and assemble with IFN-regulatory factor 9 (IRF9) to form a complex known as IFN-stimulated gene factor 3 (ISGF3), which binds the IFN-stimulated response element (ISRE) to activate transcription of IFN-stimulated genes, thereby generating an antiviral response. Figure adapted from (32) and created with BioRender (www.biorender.com).

## 1.5 Subcellular localization and non-canonical functions of cGAS and STING

It was long thought that cGAS was found only in the cytosol, where it functioned by sensing DNA from various sources to initiate an immune response (41). It was reported that cGAS was anchored to the plasma membrane through association with phosphatidylinositide phosphates and that localization elsewhere was a result of defective lipid binding (42). However, recent advances have revealed that cGAS localizes to various subcellular compartments (42-46) (Fig. 4). cGAS was found anchored to the mitochondrial membrane, where it regulated ferroptosis in hepatocellular carcinoma (43). Moreover, both nuclear localization signals (NLSs) and a nuclear export signal (NES) have been described for cGAS, indicating a role for cGAS in the nucleus (44-49).

Nuclear cGAS have been shown to be important in the recognition of human immunodeficiency virus (HIV) upon interaction with viral DNA in macrophages and dendritic cells (50). However, the functions of nuclear cGAS extend beyond those of sensing viral DNA. Nuclear cGAS has been shown to suppress homologous recombination upon double-strand breaks (DSBs) in DNA, to slow down replication forks, and to interact tightly with nucleosomes, thereby suppressing its catalytical activity (45, 51, 52). It is apparent that the localization and function of cGAS are more diverse than previously thought and likely dependent on the biological system of study. The subcellular localization of cGAS in the lung fibroblast Wi-38 cell line has yet to be elucidated.

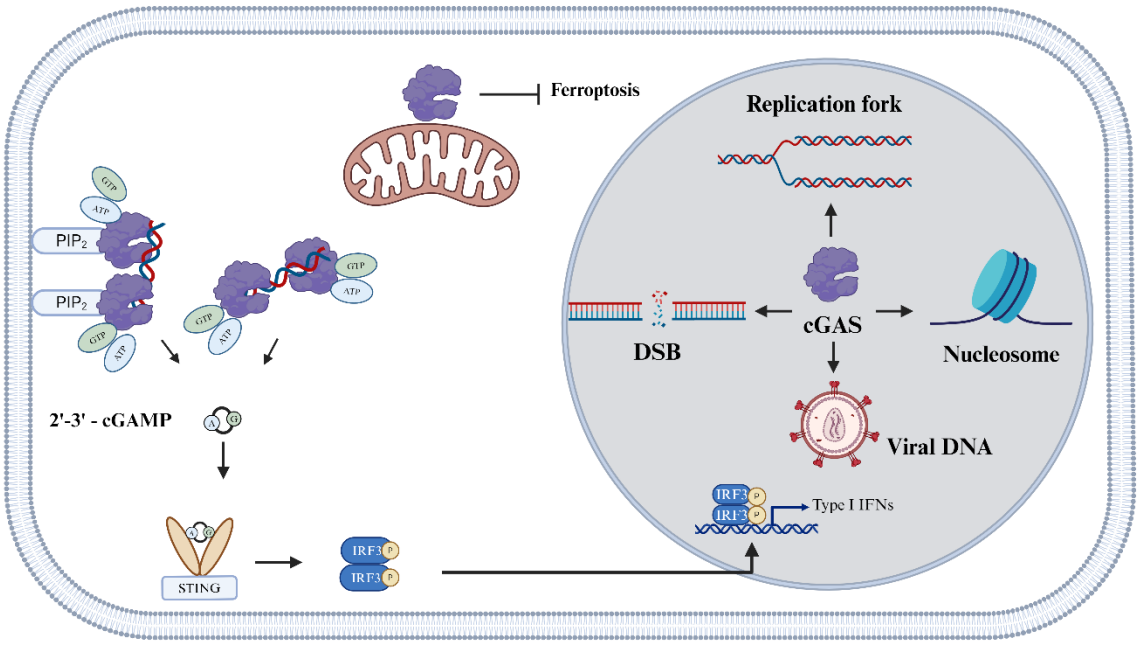


**Figure 4: Overview of cGAS subcellular localization and functions.** cGAS demonstrates diverse subcellular localizations and functions. cGAS has been identified as a DNA sensor in the cytosol, existing both as a free-floating protein and bound to the plasma membrane. Moreover, cGAS has been observed within mitochondria, where it exerts an inhibitory effect on ferroptosis. Additionally, nuclear cGAS has been implicated in various functions, including interactions with replication forks and double-strand break (DSB) sites, tethering to nucleosomes, and sensing of viral DNA. Figure created using BioRender (www.biorender.com).

The discovery that cGAS had a role in the nucleus made researchers question whether STING might have nuclear functions as well. Indeed, STING has been shown to localize to the inner nuclear membrane in some cells, where it, in a cGAS-independent manner, is involved in DNA damage repair and interacts with various nucleotide-binding partners, which regulate transcription and the type I IFN response (53-55). Moreover, when STING remains associated with the endoplasmic reticulum (ER), it can interact with PKR-like endoplasmic reticulum kinase (PERK) located on the Golgi membrane. The STING-PERK interaction facilitates the phosphorylation of eukaryotic initiation factor 2α (eIF2α), thereby establishing an inflammatory and survival-oriented translational program (56). STING can also be transported to other organelles, including the mitochondria, endosomes, and lysosomes (57). Specifically, STING was shown to serve as an adaptor of RIG-I signaling in response to infection with Japanese Encephalitis Virus, in neuronal cells, thereby linking STING directly to RNA-virus infection (58). Like cGAS, the multifaceted functions of STING remain to be fully elucidated, but it is evident that they are influenced by subcellular localization.

## 1.6 Host DNA and the cGAS-STING pathway

Under normal conditions, DNA is confined to the nucleus (nDNA) and mitochondria (mtDNA). However, under pathological conditions, DNA can be released in large quantities from these compartments to the cytosol and extracellular space (59). DNA in the cytosol serves as a DAMP, which activates DNA sensors like cGAS, subsequently contributing to efficient clearance of infection (32, 60). In contrast, DNA release and activation of cGAS-STING have also been connected to the development of the senescence and senescence-associated secretory phenotype (SASP) (56). Moreover, DNA in the extracellular space can cause sterile inflammation, contributing to the immunopathology of infection (61-63). Gain-of-function mutations in STING are common in patients with STING-associated vasculopathy with onset in infancy (SAVI), an autoinflammatory disease recognized for systemic inflammation, pulmonary fibrosis, and respiratory failure (64). Taken together, the cytoplasmic and extracellular release of DNA can both contribute to the clearance of infection through cGAS-STING, but excessive activation of this signaling axis might drive senescence and excessive inflammation.

Extranuclear sources of nDNA include micronuclei and isolated DNA structures resulting from faulty DNA replication, repair, or mitosis (59). Micronuclei comprise chromatin structures enclosed within a nuclear envelope that protrude from the nucleus in response to DSBs, unsuccessful DNA damage repair, or mitotic errors. The released nDNA may encounter cGAS through two mechanisms: nuclear cGAS may be incorporated within the micronuclei, or cytosolic cGAS may interact with exposed nDNA following the collapse of the micronuclear envelope (48, 65). Additionally, in senescent cells, nDNA has been reported to enter the cytosol through loss of nuclear integrity and through extranuclear trafficking of damaged nDNA, which activates cGAS, resulting in the persistent inflammatory state associated with senescence (66, 67). Therefore, the cGAS-STING pathway has been implicated as one of the major regulators of senescence and SASP (66).

Like nDNA, mtDNA can translocate to the cytoplasm under various stress conditions, including oxidative stress, genotoxic stress, high levels of proinflammatory factors, and structural disruption. Under such circumstances, mtDNA has the potential to activate the cGAS-STING pathway, leading to inflammation (59, 68). Altogether, while cytosolic DNA activates protective responses through DNA sensors like cGAS, its excessive release can lead to senescence, inflammation, and immunopathology, underscoring the intricate balance between immune-protection and disease progression.

## 1.7 RNA virus induced DNA damage

There are only a few examples of RNA viruses causing activation of the cGAS-STING immune axis through damage and release of nDNA and mtDNA. Two papers published in 2021 displayed how the fusion protein of SARS-CoV-2 caused syncytia formation and that this was sufficient to cause leakage of nDNA to the cytoplasm due to the mechanical disruption of the cytoskeleton and the nuclear envelope (69, 70). Another study showed that the NS4 protein of norovirus, an ssRNA virus, mediated leakage of both nDNA and mtDNA, causing robust cGAS-STING activation (71). Additionally, dengue virus, another ssRNA virus, causes the release of mtDNA to the cytoplasm, potentially through the induction of intrinsic apoptosis (72). These studies highlight how viral infection can cause DNA damage and release, thereby being crucial for an efficient antiviral response and representing an indirect mechanism of viral detection.

Although the release of DNA from the nucleus and mitochondria after RSV infection has not been shown, one paper demonstrated that RSV infection can induce DNA damage in the lung epithelial cell line, A549 (73). The authors proposed that reactive oxygen species (ROS) were generated, at least partially, from the mitochondria, which led to DNA damage. Additionally, the induction of DNA damage was linked to senescence (73). As previously touched upon, RSV is named for its ability to cause syncytia, which has been highlighted as the cause of DNA release in SARS-CoV-2 infected cells (27-29, 69, 70). Thus, the generation of ROS and the formation of syncytia in RSV-infected cells suggest that RSV infection could induce the release of nDNA and mtDNA into the cytoplasm. The misplaced DNA could activate the cGAS-STING pathway, contributing to the host response against RSV infection.

## 1.8 Aim of study

Since its discovery in 2013, cGAS has been extensively researched for its role in sensing DNA in the cytosol (74, 75). However, little is known about cGAS-STING in the immune response to RNA viruses, especially RSV. Preliminary results from our group indicate activation of the canonical cGAS-STING axis upon RSV infection in the lung fibroblast cell line, Wi-38 (76-78). However, the mechanisms of cGAS activation in RSV infected cells have never been studied. Likewise, cGAS subcellular localization in Wi-38 has yet to be described. Hence, the primary objective of this thesis was twofold: firstly, to investigate the subcellular localization of cGAS following RSV infection in the lung fibroblast cell line, Wi-38; and secondly, to

examine the potential presence of DNA within the cytosol and extracellular space. Specifically, the following aspects were pursued:

- Investigate cGAS-STING signaling in response to RSV infection in Wi-38 cells in a time-dependent manner.
- Examine the subcellular localization of cGAS in non-infected and RSV-infected Wi-38 cells to determine the impact of viral infection on cGAS distribution.
- Evaluate the induction of γH2AX, as a marker for double-stranded breaks (DSBs) in nuclear DNA, in Wi-38 cells following RSV infection.
- Investigate the presence of host DNA and γH2AX in the cytoplasm and host DNA in the extracellular space of Wi-38 cells following infection with RSV.
- Evaluate the integrity of the nuclear lamina following RSV infection.
- Determine the kinetics of γH2AX expression and host DNA release to the extracellular milieu in a model of the post-acute phase of RSV infection in Wi-38 cells.

# 2. Methods

## 2.1 Cells and culture conditions

The cell lines Wi-38 (Sigma-Aldrich, CB90020107) and HEp-2 (ATCC, CCL-23) were utilized in this project. Wi-38 cells were cultured in Dulbecco's Modified Eagle Medium (DMEM, Sigma-Aldrich, D6429) supplemented with 10% Fetal Bovine Serum (FBS) (Sigma, #F7436) and 1% Penicillin-Streptomycin (Pen/Strep) (Gibco, #15070063). The Hep-2 cells were cultured in DMEM with 10% FBS, 1% Pen/Strep, and 0,3% L-glutamine (Sigma, #G7513). Both cell lines were kept at 37ºC in 5% $CO_2$ and subcultured at 80-90% confluence.

Cells were washed in 1X Phosphate Buffer Saline (Gibco, # 18912014) and detached with Trypsin-EDTA (Sigma, #T3924) prior to subculturing. Trypsination was blocked by the addition of the growth medium, and the excess trypsin was removed by centrifuging the cell suspension at 1500 rpm for 5 min, before resuspending the pellet in fresh medium. Cells were either seeded into T75 flasks or seeded out for experiments.

## 2.2 *In vitro* RSV infection and diABZI stimulation

The RSV A2 strain, sourced from B. van den Hoogen at the Erasmus Medical Center in Rotterdam, Netherlands, was utilized for *in vitro* RSV infection experiments on WI-38 and HEp-2. Cells were infected at a confluency of 70-80% at a multiplicity of infection (MOI) of either 1 or 3, as denoted in the result section. To optimize viral growth, the Opti-MEM® I Reduced Serum Medium (Gibco, #31985047), supplemented with 2% FBS and 0.3% L-glutamin, was used during infection. After infection, cells were incubated at 37ºC in 5% $CO_2$ for varying durations, as denoted in the results section.

diABZI is a potent STING agonist, which, similarly to cGAMP, activates STING *in vitro* and *in vivo* and was used as a positive control (79). HEp-2 and Wi-38 cells were stimulated with 10 µM diABZI for 4 and 3 h, respectively. To increase solubility, diABZI was first diluted in dimethyl sulfoxide (DMSO) before being diluted in the growth medium of the respective cell line.

## 2.3 Recombinant green fluorescent protein-expressing RSV

To visualize infected cells, a recombinant green fluorescent protein (GFP)-expressing RSV (rgRSV) provided by Mark E. Peeples, was used for infection in Wi-38 cells. Briefly, rgRSV was constructed by inserting GFP (Life Technologies, Gaithersburg, Md.) as the first gene of the full-length positive-sense cDNA clone of the RSV A2 strain, MP224 (80). Next, the plasmid containing the full RSV genome was transfected together with four plasmids containing essential genes for RSV replication (N, P, L, and M2-1) into HEp-2 cells. In addition, the recombinant vaccinia virus MVA-T7 provided a T7 RNA polymerase, which drove the expression from the plasmids (81). The released infectious virus was amplified in HEp-2 cells. rgRSV was reported to reproduce efficiently at titers near the level of the wild-type strain, with similar levels of syncytia formation (82).

Prior to this project, the rgRSV stock was propagated, isolated, and titrated by laboratory personnel. 4,5 million HEp-2 cells were seeded in T175 flasks, and infected at 40-50% confluency with rgRSV at a MOI of 0,02 in DMEM with 2% FBS, 1% Pen/Strep and 0,3% L-glutamine medium. After a 3 h incubation period, the virus was removed and fresh medium was added and left to incubate for five more days, before the medium was changed again. On the following day, cells were inspected by microscopy, and all cells appeared infected by emitting green fluorescence. The cells were then frozen at -80ºC. Upon thawing, the supernatant was transferred to a 50 mL tube, and subjected to a 5 min centrifugation step at 4ºC. A second tube was filled with 1 mL 60% sucrose, before 15 mL of the supernatant was added. The sucrose-virus suspension was centrifuged for 2 h at 26000 rpm at 4ºC. The assumption was made that the virus resided primarily in the sucrose and lower medium-layer portion. Consequently, the upper 11 mL was discarded, and the remaining residues were transferred to a new tube containing 1 mL of 60% sucrose and 4 mL of 30% sucrose. The tube was filled with PBS. Another 2 h centrifugation at 26000 rpm and 4ºC step was performed. The PBS and upper part of the 30% sucrose phase were removed. The remaining suspension consisting of mostly 60% sucrose and virus was diluted 1:1 in OptiMEM supplemented with 2% FBS and frozen at -80ºC.

For determining the viral titer, 20.000 HEp-2 cells were seeded on a 96-well plate in 200 µL medium. The following day, rgRSV was diluted 1:100 in 2%FBS/DMSO, followed by a serial dilution by a factor of 10, to yield 8 different concentrations. HEp-2 cells were washed in PBS, before addition of 200 µL of each dilution of the virus. The infected cells were incubated for 3 days at 37ºC in 5% $CO_2$, before being assessed by fluorescence microscopy for focus forming units (FFU). The FFU/mL was calculated by the following formula:

$$\frac{FFU}{mL} = \frac{Average\ number\ of\ foci}{Volume\ of\ virus\ added\ x\ Dilution\ factor}.$$

## 2.4 Subcellular fractionation

Subcellular fractionation is a method used to study the subcellular localization of molecules. The method is utilized for yielding fractions enriched for molecules from specific subcellular compartments. Specifically, we aimed to yield pure nuclear and cytosolic fractions, as well as a crude mitochondrial fraction.

The protocol for subcellular fractionation was adapted from (83). 1,8 million Wi-38 cells were seeded on a 10cm$^2$ dish, and infected with RSV for 48 h and 72 h. Cells were then washed in PBS, tyrpsinated, and pelleted. The pellet was washed in 10 mL PBS and resuspended in 150 µL digitonin lysis buffer consisting of 150 mM NaCl, 50 mM HEPES pH 7.4, 25 ug/mL Digitonin, 1% phosphatase inhibitor cocktails 2 and 3 (PIC 2 and 3) (Sigma, #P5726 and #P0044 respectively), and 2% of cOmplete™, Mini, EDTA-free Protease Inhibitor Cocktail at 1:50 (Sigma, #1183617000). The suspension was incubated on a head-to-tail rotator for 10 min at 4ºC, before centrifugation at 2000 g at 4ºC for 10 min. The resulting pellet was the nuclear- and mitochondrial fractions, which were stored on ice for later processing. The supernatant went through three rounds of 20 min centrifugation at 20.000 g and 4ºC, to yield a pure cytosolic fraction which was split for Western blotting and DNA isolation.

The pellet consisting of the nuclear- and mitochondrial fractions was washed in 1 mL PBS, and centrifuged for 5 min at 16.000 g. Next, the pellet was resuspended in 150 µL NP-40 lysis buffer consisting of 150 mM NaCl, 50 mM HEPES pH 7.4, 4,1% NP-40, 1% PIC 2 and 3, and 2% of cOmplete™ protease inhibitor cocktail, and centrifuged again at 7000 g for 10 min. The supernatant was the crude mitochondrial fraction which was stored for Western blot analysis. The pellet was washed in 1 mL PBS and resuspended in 150 µL RIPA lysis buffer consisting of 50 mM Tris HCl pH 8.0, 200 mM NaCl, 1 % NP-40, 0.5 % Sodium Deoxycholate, 0.05 % SDS, 2 mM EDTA, 1% PIC 2 and 3, and 2% cOmplete™ protease inhibitor cocktail. The final suspension was the nuclear fraction which was split for DNA isolation and Western blot analysis.

## 2.5 Western blotting

Western blotting is a semi-quantitative method of protein detection. Briefly, cell-lysates are loaded onto a sodium dodecyl sulfate polyacrylamide gel and separated by molecular weight by electrophoresis (SDS-PAGE). The proteins are then transferred from the gel onto a synthetic membrane. The membrane is incubated in a blocking buffer to prevent the non-specific binding of antibodies. Next, the membrane is incubated with primary antibodies specific for the protein of interest, followed by incubation with a secondary antibody. The secondary antibody is fluorescently labeled for direct detection or enzyme-conjugated for signal generation via a substrate reaction.

Herein, 80.000 HEp-2 cells or 70.000 Wi-38 cells were seeded on 24-well plates for Western blotting. Cell lysis was conducted using a lysis buffer containing 50 mM Tris-HCl, 150 mM NaCl, 10% Glycerol, 1% Triton X-100, and 2 mM EDTA, supplemented with 1% phosphatase inhibitors PIC 2 and PIC 3 (Sigma-Aldrich, P5726 and P0044), along with 2% cOmplete™ protease inhibitor cocktail (Roche Diagnostics). The lysates were centrifuged to get rid of debris. To denature the proteins and break disulfide bonds, the lysates were added to a 4X lithium dodecyl (LDS) sample buffer (Invitrogen NuPAGE) containing 10% dithiothreitol (DTT) and heated to 70 ºC while shaking for 10 min. Then, the samples, SeeBlue™ Prestained Protein Standard (Invitrogen, LC5925) and Magic Mark™ XP Western Protein Standard (Invitrogen NuPAGE, LC5602) were loaded onto a 4-12% Bis-Tris gel (Invitrogen NuPAGE, NP0322BOX), before being ran in 1X MOPS at 200 V for ~75 min. Following separation, the proteins were transferred to an iBlot™ 2 Nitrocellulose Mini Transfer Stacks (Invitrogen, #IB23002) or iBlot™ 2 Nitrocellulose Regular Transfer Stacks (Invitrogen #IB23001) by iBlot®2 Gel Transfer device (Invitrogen).

After transfer, the nitrocellulose membrane was rinsed in 1X Tris-buffered saline (TBS) and blocked for 1 h in Intercept™ (TBS) Blocking Buffer (LI-COR Biosciences, #927-60001). The membrane was then washed 3 x 5 min in 1X TBS with 0,1% Tween-20 (TBS-T), before the addition of a primary antibody, diluted in a 1:1 solution of TBS-T and Intercept™ (TBS) Blocking Buffer, at 4 ºC overnight. The membrane was washed 3 x 5 min in TBS-T the following day, before being incubated with a secondary antibody for 1 h at room temperature (RT). A list of the primary and secondary antibodies used, and the dilution factors can be found in the appendix (appendix table A1 and A2, respectively). Finally, the membrane was washed 2 x 5 min in TBS-T and 1 x 10 min in TBS, before drying and subsequently reading with LI-

COR Odyssey Imager (LI-COR Biosciences). Image Studio version 5.2. Software was used for densitometry quantification.

## 2.6 Quantitative polymerase chain reaction

Quantitative polymerase chain reaction (qPCR) is a method used for amplification and quantification of DNA fragments in real-time. In general, DNA is isolated from a sample, and is set to undergo between 15 and 40 rounds of denaturation, annealing and elongation. Specific primer pairs are used to amplify the gene of interest. To quantify the total content of DNA in the sample, fluorescent markers which emits fluorescence when bound to dsDNA, are used. After multiple rounds of amplification, the fluorescent signal exceeds that of the background level. This is determined the cyclic threshold (Ct) and is used for quantitative analysis.

DNA was isolated from a cell pellet, a nuclear fraction, a cytosolic fraction, and the supernatant (the harvested growth medium), using the Qiagen blood and tissue kit (Qiagen, 69504). The manufacturer's protocol: "Protocol: Purification of Total DNA from Animal Blood or Cells (Spin-Column protocol)", was followed with the following modifications: Initially, the cell pellet, 25 µL of the nuclear fraction, or 75 µL of the cytosolic fraction, were resuspended in PBS to a total volume of 200 µL, before 20 µL of Proteinase K was added to the suspension. Proteinase K was added directly to 200 µL of the supernatant. Also, in the final elution step, 35 µL of the AE buffer was used instead of the recommended 200 µL to increase the final DNA concentration.

All samples were analyzed in triplicates to ensure reproducibility. Each qPCR reaction mixture consisted of 10 µL of PerfeCTa(R) SYBR® Green Fast Mix (QuantaBio, 733-1386), 5,5 µL DNase-free water, 1 µL of each primer **(**appendix table. A3**)**, and 2,5 µL of the sample DNA. The reactions were set up in a 96-well plate and performed on a StepOnePlus Real-Time PCR system (Applied Biosystems). The qPCR cycling conditions were repeated cycles of denaturation at 95°C for 3 sec and annealing and elongation at 60°C for 30 sec. To detect potential contamination, a negative control for each primer pair was included. In these, DNase-free water was added in replacement of DNA. Quantification of DNA content was performed using the ΔΔCt-method. Briefly, the Ct value obtained from the amplification of the target gene was compared to that of an endogenous control and to the untreated sample. All qPCR results are presented as fold change.

## 2.7 Staining for fluorescence microscopy

Fluorescence microscopy is a light-microscopy-based technique in which target molecules are labeled with a fluorophore, allowing for visualization (84). The fluorophores could, among others, be antibodies conjugated to a fluorescent probe, fluorescent dyes, or fluorescent proteins. The principle of fluorescence microscopy is that you illuminate the samples with light of a given wavelength, which is absorbed by the fluorophore. The fluorophore will then emit light of a different wavelength, which can be detected by a detector (84).

15.000 cells were seeded out on an SPL Life Sciences 8-well cell culture slide with Flux bottom (SPL, 30508) and were allowed to attach overnight. Subsequently, cells were either maintained untreated in the OptiMEM/2%FBS + glutamine medium or subjected to infection with RSV or rgRSV. All cells were simultaneously fixated 48 h post-infection in 4% paraformaldehyde (Sigma-Aldrich, P6148) and incubated on ice for 10 min. After fixation, cells were washed 3 x 5 min in PBS before permeabilization and blocking of nonspecific binding sites were achieved by adding a buffer consisting of PBS with 10% FBS, 2,5% BSA (Sigma-Aldrich, A7030), and 0,3% Triton X-100 for 1 h in RT.

Next, primary antibodies diluted in a buffer consisting of PBS with 10% FBS and 2,5% BSA were added and left overnight at 4ºC (appendix A1). The morning after, cells were washed 3 x 5 min in PBST (PBS/1% Tween-20), followed by 1 h incubation in RT with the secondary antibodies diluted in the dilution buffer (appendix A2). Another round of 3 x 5 min washing in PBS was performed, followed by the addition of the DNA dye, DAPI (4′,6-diamidino-2-phenylindole) (Sigma-Aldrich D9542) diluted 1:1000 in PBS, for 20 min at RT. The samples underwent a final triple washing step in PBS for 10 min each before the Flux bottom of the wells was removed and mounted between a mounting slide and a cover slip, using the Fluoromount-G™ mounting medium (Thermo Fischer Scientific, 00-4958-02). The slides were left to dry for 1 h before microscopy analysis.

## 2.8 Confocal Microscopy

Confocal microscopy is a fluorescence microscopy technique used to increase resolution compared to standard wide-field microscopy. The fundamental concept in confocal microscopy is that illumination and detection are focused on one spot in the sample, which moves across the sample to build a complete image (85). Enhanced resolution compared to wide-field

microscopy is achieved by rejecting out-of-focus light using a pinhole, which only allows passage of light emitted from the focus plane (85).

Fixated and mounted samples were imaged by a Zeiss LSM510 Meta laser confocal microscope (Carl Zeiss, Oberkochen, Germany) using a 63x/1.4 oil immersion objective and detection at λ = 405/420-480nm (DAPI), λ = 488/505-550nm (GFP), λ = 561/575-615nm (Alexa Fluor™ 555), and λ = 633/>650 (Alexa Fluor™ 647). The pinhole was kept at 1 airy unit to achieve the best resolution. Laser power was adjusted to minimize photobleaching while ensuring sufficient signal intensity, typically set to 20% below the maximum power. Microscope gain settings were optimized for each target, maximizing the signal without achieving detectable levels in associated isotype controls. Single-labeled controls were used in the initial experiments to address and minimize the level of bleed-through between the fluorophores. Imaging settings remained identical across all experiments.

## 2.9 Image analysis

ImageJ 2.14.0/1.54f was used for manual assessment of cGAS distribution, γH2AX foci, and rgRSV-positive cells, as stated in the results section. CellProfiler 4.2.6 was used for defining the nucleus and cytoplasm, measurements of intensity, and co-localization analysis. CellProfiler's global thresholding strategy, with minimum cross-entropy, was used to define the nuclei from the DAPI staining. The cytoplasm of each cell was defined by expanding the nuclei-boundary by an arbitrarily 60 pixels in the X and Y directions and thereafter subtracting the nuclei, as shown in figure 6a. An area of 60 pixels was chosen to cover enough cytoplasmic area to show meaningful differences between treated and untreated samples while avoiding including irrelevant portions of the image. Pixel intensity normalization from the original 8-bit scale (0-255) to a range of 0 to 1 was applied for practicality and simplicity in data interpretation without altering the analytical outcomes. The mean fluorescent intensity of each object, rather than the integrated intensity, was used for analysis, to account for any differences in are of the nuclei or cytoplasm. The data are presented as the average mean intensity of all objects in the group.

Mander's method for co-localization was used for co-localization analysis. This method yields two coefficients: the fraction of pixels positive for protein A, which are also positive for protein B. And the fraction of pixels positive for protein B, which are also positive for protein A (86). A coefficient of 1 would indicate complete co-localization, while 0 would indicate no co-

localization. To separate the fluorescent signal from background noise, Costes' thresholding strategy was utilized (87). Costes' thresholding strategy utilizes a statistical approach to determine the optimal threshold for a pixel to be identified as foreground, thereby improving reproducibility. Raw images were used during all analyses. However, the brightness and contrast of the images presented are consistently enhanced in ImageJ for visualization purposes.

## 2.10 Statistical analysis

Statistical analysis was performed in GraphPad Prism 10.2.2 software. When comparing two groups, the student's two-tailed T-test was used. For comparison between multiple groups, a one-way ANOVA with Tukey's honest significance difference test was used. All quantitative data are presented as mean ± SD. The significance level was set to $\alpha = 0.05$. Significant results are denoted with P-values. Non-significant results are not annotated.

# 3. Results

## 3.1 RSV infection induces cGAS-STING signaling in HEp-2 and Wi-38 cells

Preliminary work from our group has demonstrated cGAS-STING activation in response to RSV infection (Lance, Mathilde). To verify these findings, HEp-2 and Wi-38 cells were infected with RSV at a MOI of 3 and assessed at different time points ranging from 12 to 72 h. Additionally, the STING agonist, diABZI was used as a positive control. Protein expression of cGAS, STING and other known downstream proteins in the canonical signaling pathway was assessed by Western blotting (Fig. 5).

RSV infection caused a continuous increase in STING and cGAS expression, and STING phosphorylation (Ser366) in both cell lines, with STING phosphorylation being delayed in Wi-38 cells compared to HEp-2 cells. Moreover, phosphorylation of TBK1 (Ser172) and IRF3 (Ser396) was seen in both cell lines, where phospho-IRF3 expression increased before STING phosphorylation in Wi-38 cells, indicating signaling through other pathways. Overall, these results support a role for cGAS-STING in the innate response to RSV, especially at the later time points of infection. Due, to the superior physiological relevance of Wi-38 cells, work in HEp-2 cells was discontinued.

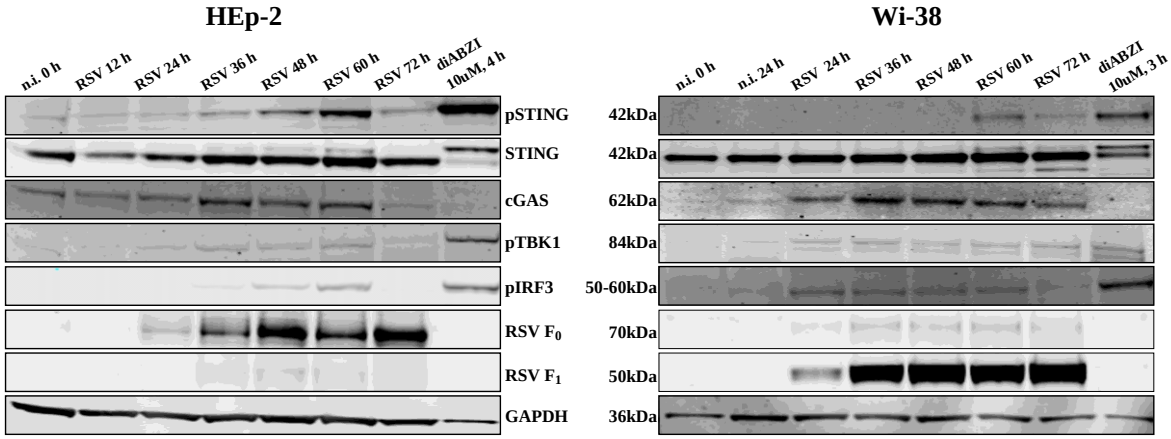


**Figure 5: The cGAS-STING axis is activated upon RSV infection.** The Western blots depicts the kinetics of activation of the cGAS-STING signaling pathway at various time points in non-infected cells (n.i.) and following RSV infection, utilizing a multiplicity of infection of 3 in both HEp-2 and Wi-38 cells. As a positive control, diABZI, a potent STING agonist, was included. The Western blot from HEp-2 is representative of one experiment, while the Western blot from Wi-38 are representative of two biological replicates.

## 3.2 cGAS is present in the nuclei of non-infected cells, while also being detectable in the cytoplasm of RSV-infected cells

The distribution of cGAS in the nucleus and cytoplasm appears to be cell-type dependent (46). Therefore, we wanted to examine the subcellular localization of cGAS in the nucleus and cytoplasm of Wi-38 cells following RSV infection.

To determine the distribution of cGAS between the cytoplasm and nucleus, Wi-38 cells were infected with RSV at a MOI of 3 for 48 h, before being fixated, stained for cGAS, and assessed by confocal microscopy. The DNA marker, DAPI, was used to define the nucleus, while the cytoplasm was defined as an area of 60 pixels surrounding the nucleus, as depicted in figure 6a. Cells were manually scored as having predominantly nuclear localization (N), predominantly cytoplasmic localization (C), or a combination (N+C) (Fig. 6b), as previously done by Son and colleagues (47). In non-infected cells, cGAS was present almost exclusively in the nuclei, while showing both nuclear, and nuclear and cytoplasmic localization in RSV-infected cells (Fig. 6c). These results were further supported by measurements of the fluorescent signal in the nuclei and cytoplasm. Non-infected cells produced no fluorescent signal in the cytoplasm but stained weakly positive for cGAS in the nuclei. After RSV infection, a 4- and 38-fold intensification of the fluorescent signal was measured in the nuclei and cytoplasm, respectively, illustrating both nuclear and cytoplasmic presence of cGAS (Fig. 6d and e).

To evaluate the subcellular localization of cGAS in Wi-38 cells by an additional approach, Wi-38 cells were infected with RSV at a MOI of 3 for 48 and 72 h. Cells-lysates were separated into three distinct fractions: cytosolic, mitochondrial, and nuclear, which were enriched with proteins localized to the respective intracellular compartments (appendix Fig. A1). Protein expression was assessed by Western blotting and compared to an endogenous control for the respective fraction (Fig. 6f). cGAS expression in the nucleus decreased slightly 72 h post-infection, while it in the cytoplasm increased multifold above the levels in non-infected cells (Fig. 6g), thereby supporting the microscopy findings. Together, the microscopy and subcellular fractionation results show that cGAS is present primarily in the nuclei of non-infected Wi-38 cells, while being present both in the cytoplasm and the nuclei after RSV infection.

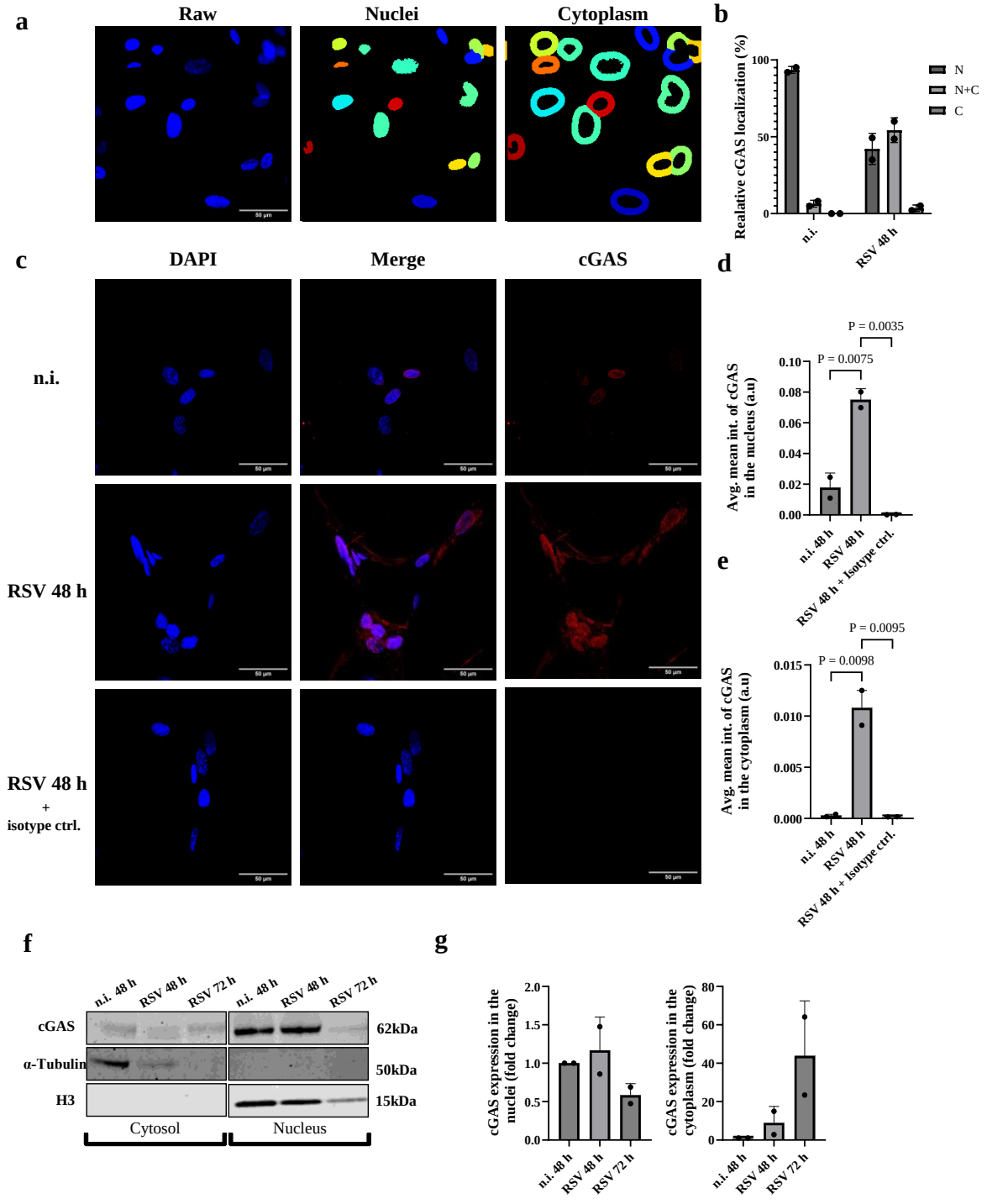


**Figure 6: RSV infection affects the subcellular distribution of cGAS**. **(a)** Images depicting the cytoplasm, defined as a region of 60 pixels surrounding the nuclei. **(b)** Representative images from two independent experiments show cGAS localization in non-infected (n.i.) ($n_1$=101, $n_2$=257) and RSV-infected cells ($n_1$=143, $n_2$=93) at a multiplicity of infection (MOI) of 3. Anti-Rabbit IgG served as a negative control for cGAS detection ($n_1$=22, $n_2$=125). **(c)** Cells from the two biological replicates were scored as having primarily nuclear (N), nuclear and cytoplasmic (N+C), or cytoplasmic (C) localization of cGAS. **(d, e)** The fluorescent signal of cGAS was measured in the nuclei and the cytoplasm as defined in **a**. The fluorescent signal is presented as the average mean intensity of all cells across the two replicates. **(f)** Wi-38 cells were infected with RSV at a MOI of 3 for 48 and 72

h. The lysates were enriched into three fractions: the cytosol, mitochondria, and nucleus, each enriched for proteins from the respective subcellular compartment. A representative Western blot from two experiments illustrating cGAS distribution in the nuclei and cytosol, alongside α-tubulin as a cytosolic marker and H3 as a nuclear marker, is presented. **(g)** Expression of cGAS in the cytosolic and nuclear fractions is related to the marker of the respective fraction and presented as a fold change from n.i. cells. All quantitative results are presented as mean ± SD. Statistical analysis: One-way ANOVA with Tukey's multiple comparison test. P-values of significant results are presented in graph. Significance level $\alpha < 0.05$.

## 3.3 Recombinant GFP-expressing RSV and activation of the cGAS-STING immune axis.

Next, we wanted to explore if cGAS was present in the cytoplasm only in the subset of Wi-38 cells that were infected with RSV. To assess which cells were infected, a recombinant green fluorescent protein (GFP)-expressing RSV (rgRSV) was used. Previously performed in-house propagation, isolation, and titration of the rgRSV-stock, showed results ranging from a concentration of 625.000 FFU/mL to 2.750.000 FFU/mL. As a result, the average of the two measurements, 1.700.000 FFU/mL, was used for the initial experiment.

First, we wanted to determine the fraction of Wi-38 cells that were infected 48 h post infection. Wi-38 cells were infected with rgRSV at a MOI of 3 and assessed by confocal microscopy (Fig. 7a). The cells which emitted a fluorescent signal greater than that of the background signal in wild-type RSV infected cells (denoted as RSV), were considered infected. In total, 74% of the cells were infected 48 h after addition of the virus (Fig. 7b). Notably, at the time of fixation, the confluency of the rgRSV-infected cells was ~40%, compared to ~60% in those infected with wild-type RSV, indicating higher viral titers than initially assumed.

Due to uncertainty in the viral titers, we wanted to assess the response through the cGAS-STING axis after infection with rgRSV. To do so, Wi-38 cells were infected with both rgRSV and RSV at a MOI of 1 and 3 for 48 h and analyzed by Western blotting (Fig. 7c). For rgRSV, three different concentrations were used for the calculations. Interestingly, rgRSV showed an increased STING phosphorylation (Ser366), compared to RSV infected cells. Additionally, phosphorylated IRF3 (Ser396) showed a markedly distinct pattern in rgRSV cells compared to RVS.

The expression of the RSV fusion protein $F_1$ and its larger precursor form, $F_{0,}$ were quantified relative to the housekeeping protein Glyceraldehyde 3-Phosphate Dehydrogenase (GAPDH) (Fig. 7d and e).

Altogether, due to uncertainty in the viral titer, as well as the response of the target cells which differed from that observed after infection with RSV, further work with rgRSV was discontinued.

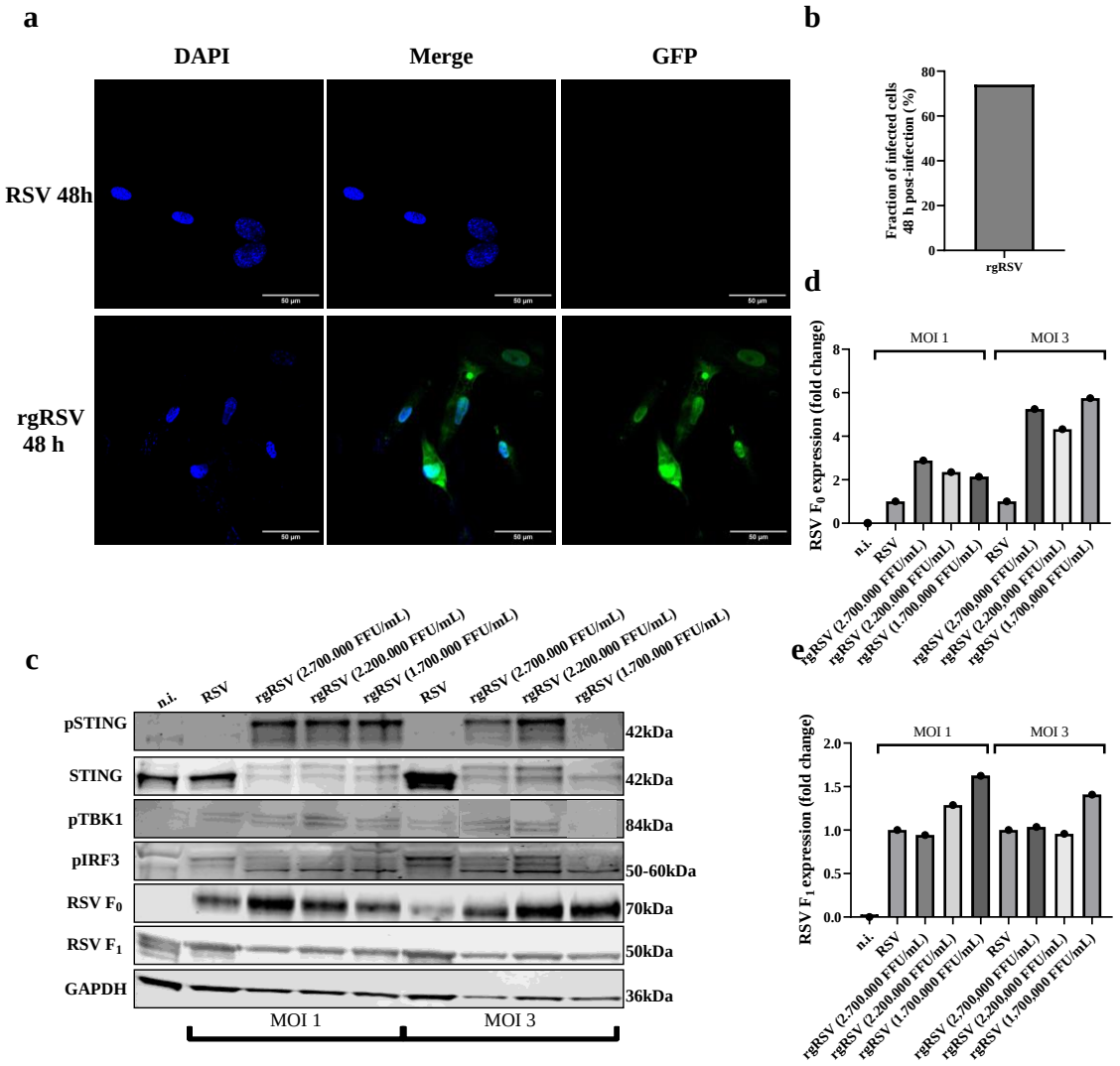


**Figure 7: Fraction of cells infected with recombinant green fluorescent (GFP) protein-expressing RSV (rgRSV) and rgRSV-induced activation of proteins in the cGAS-STING immune axis. (a)** Wi-38 cells were infected with wild-type RSV and rgRSV at an intended multiplicity of infection (MOI) of 3 for 48 h and assessed by confocal microscopy, to investigate the fraction of total cells being infected. The wild-type RSV served as a negative control, to account for background fluorescence. **(b)** All cells from one experiment were assessed (n=197), and the cells emitting a fluorescent signal stronger than that of WT RSV-infected cells were categorized as infected. **(c)** Because of low the confluency in rgRSV compared to RSV, indicative of wrong in viral titers in the experiment described in **a,** an additional experiment to investigate the cellular response to rgRSV was performed. Wi-38 cells were infected with rgRSV at MOI of 1 and 3. The amount of virus used for each condition was calculated from different FFU/mL concentrations, as indicated in the figure. **(d, e)** The viral load was assessed

by quantifying the RSV $F_0$ protein and its cleaved mature form $F_1$ in relation to GAPDH. The results are presented as fold-change from cells infected with WT RSV at identical MOI.

## 3.4 The levels of γH2AX increased following RSV infection

Induction of DSBs, followed by misplacement of self-DNA has been reported to activate cGAS after SARS-CoV-2 infection (70). Our observation of that cGAS partially localizes to the cytoplasm of RSV-infected Wi-38 cells, and the previously reported RSV induced DNA damage in A549 cells, led us to ask if RSV-infection cause DNA damage in Wi-38 cells as well (73).

To evaluate the presence of DNA DSBs, we stained Wi-38 cells for the DSB marker γH2AX and inspected the cells by confocal microscopy (Fig. 8a) (88). Due to the formation of γH2AX-foci at the site of DSBs, we examined cells from across 3 experiments by the number of foci in the nuclei. Cells were defined as positive if they had $\geq$5 γH2AX foci. In non-infected cells, ~6% of the cells were positive, while the number rose to ~53% 48 h after RSV infection (Fig. 8b). To further confirm the induction of DSBs following RSV infection, a kinetic experiment was designed and assessed by Western blotting (Fig. 8c). Here, γH2AX increased almost 2000-fold over the level in non-infected cells, with a rapid increase between 24 h and 36 h post-infection (Fig. 8d). These results show that RSV infection increases the levels of γH2AX, indicating DNA DSB induction in Wi-38 lung fibroblasts.

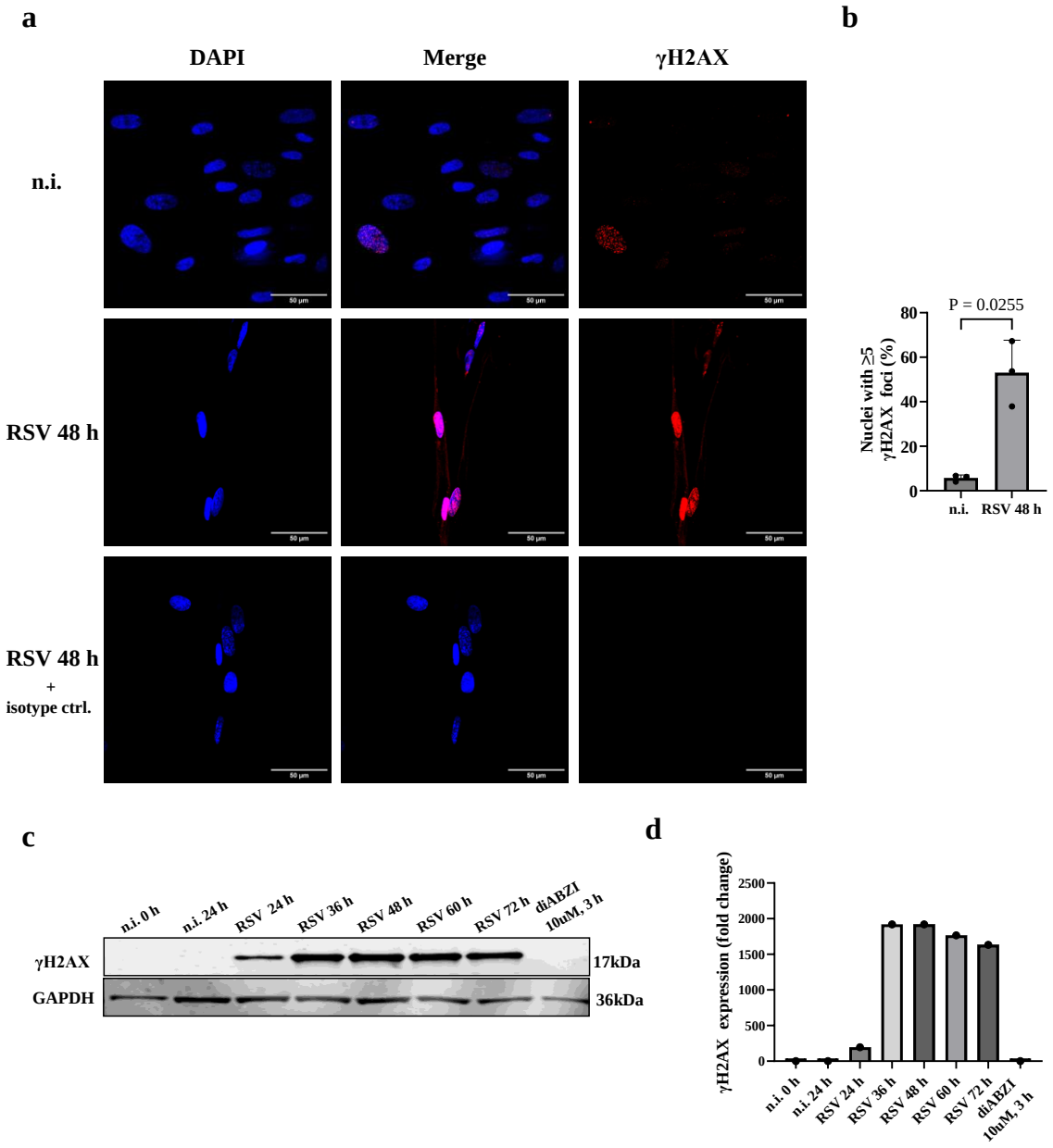


**Figure 8: Induction of double strand breaks in nuclear DNA following RSV infection. (a)** Representative images from three independent experiments show γH2AX in non-infected (n.i.) ($n_1$=114, $n_2$=203, $n_3$=96) and RSV-infected cells at an MOI of 3 ($n_1$=57, $n_2$=122, $n_3$=96). Anti-mouse IgG1 served as a negative control for γH2AX detection ($n_1$=54, $n_2$=83, $n_3$=112). **(b)** The number of γH2AX-foci within each nucleus was counted, and cells with ≥5 foci were categorized as positive. **(c)** A Western blot showing γH2AX expression together with the endogenous control GAPDH after infection with RSV. **(d)** Quantification of the Western blot depicted in **c.** All quantitative results are presented as mean ± SD. Statistical analysis: Two-tailed Student's t-test. P-values of significant results are presented in graph. Significance level $\alpha < 0.05$.

## 3.5 γH2AX, DAPI, nDNA and mtDNA are detectable in the cytoplasm after RSV infection

Following the identification of RSV induced DSBs in Wi-38 cells, we asked if DNA was localized to the cytoplasm where it could serve to activate cytoplasmic cGAS. Consequently, we aimed to determine whether γH2AX, DAPI, nDNA, and mtDNA is present in the cytoplasm of Wi-38 cells after RSV infection.

To determine the subcellular localization of γH2AX and DAPI, cells were infected with RSV before immunofluorescence staining and confocal microscopy (Fig. 9a), Like for cGAS, the cytoplasm was defined as an area of 60 pixels around the nuclei (shown in figure 6a). The fraction of cells which stained positive for γH2AX in the cytoplasm was counted (Fig. 9b). On average, 68% of Wi-38 cells stained positive for γH2AX in the cytoplasm by visual examination 48 h after infection. Additionally, quantitative measurements of the fluorescent signal showed γH2AX to be present in the cytoplasm of infected cells, but not in non-infected cells (Fig. 9c). Likewise, the fluorescent signal from DAPI in the cytoplasm was higher in RSV infected cells, compared to non-infected cells, indicative of nDNA in the cytoplasm (Fig. 9d). To investigate the cytoplasmic presence of γH2AX by an additional method, we infected cells with RSV at a MOI of 3 for 48 and 72 h, before we enriched three fractions for proteins from the respective compartment (as described in section 2.4) and compared protein expression by Western blotting. γH2AX was detectable in the cytosolic fraction 72 h after infection, despite a decrease in α-tubulin expression due to low cell confluency (Fig. 9e and 9f).

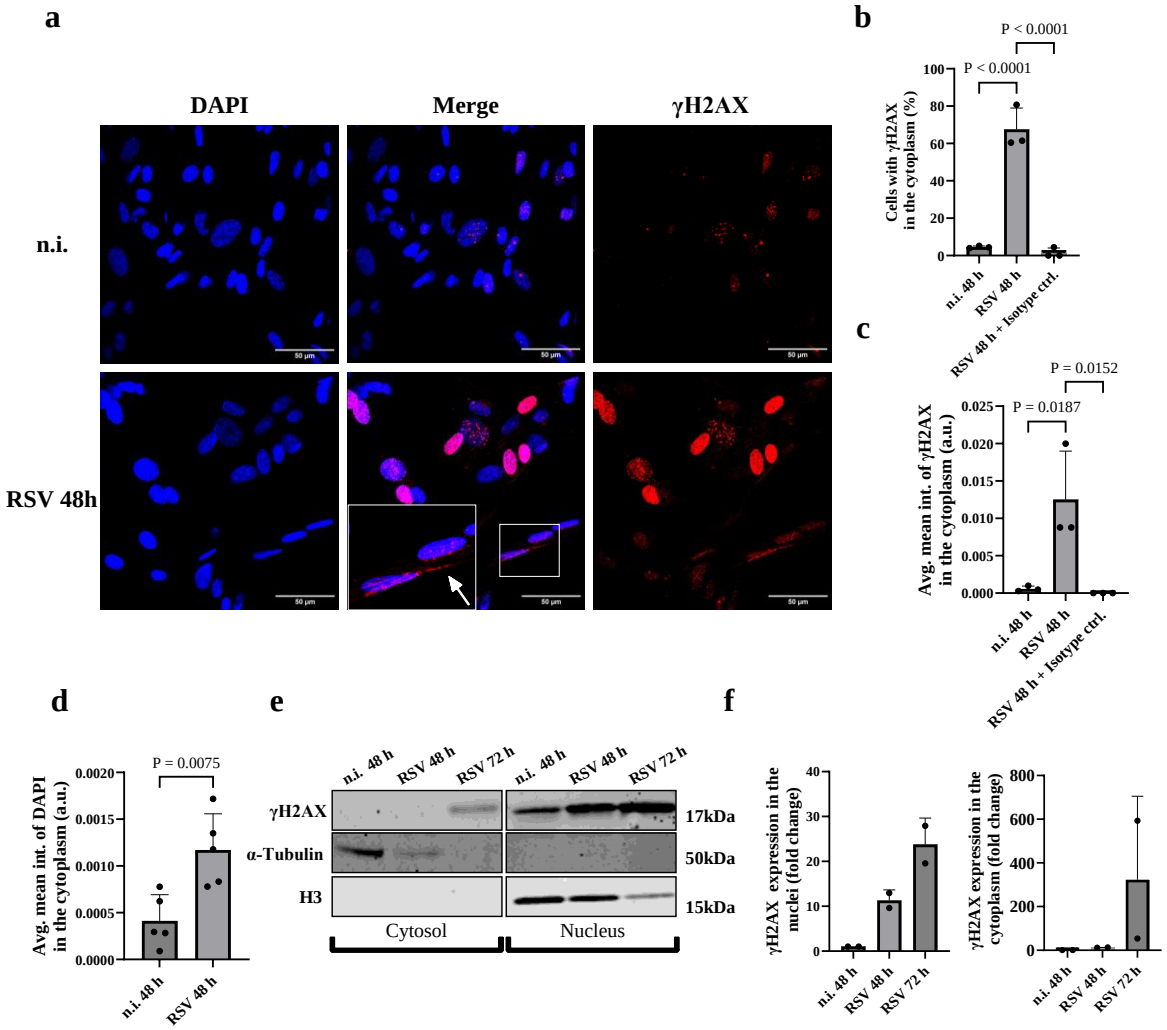


**Figure 9: γH2AX is detectable in the cytoplasm after RSV-infection. (a)** Representative images from three independent experiments show γH2AX in non-infected (n.i.) ($n_1$=114, $n_2$=203, $n_3$=96) and RSV-infected cells at a MOI of 3 ($n_1$=57, $n_2$=122, $n_3$=96). In addition, cells stained for a mouse IgG1 isotype control were assessed ($n_1$=54, $n_2$=83, $n_3$=112). **(b)** The number of cells with γH2AX in the cytoplasm was counted and presented as a fraction of total cells. **(c)** The fluorescent signal of γH2AX was measured in the cytoplasm, and the signal is presented as the average mean intensity of all cells across the three biological replicates. **(d)** Likewise, the fluorescent signal of DAPI in the cytoplasm was measured in n.i. cells ($n_1$=114, $n_2$=203, $n_3$=96, $n_4$=101, $n_5$=257) and RSV-infected cells ($n_1$=57, $n_2$=122, $n_3$=96, $n_4$=143, $n_5$=93) from five biological replicates. **(e)** Wi-38 cells were infected with RSV at a MOI of 3 for 48 and 72 h before they were enriched in three fractions for proteins in the cytosol, mitochondria, and nucleus. A representative Western blot from two experiments illustrating γH2AX distribution in the nuclei and cytosol, alongside α-tubulin as a cytosolic marker and H3 as a nuclear marker, is presented. **(f)** The expression of γH2AX in both replicates was quantified relative to the respective marker for each fraction and presented as a fold change from n.i. cells. All quantitative results are presented as mean ± SD. Statistical analysis: Two-tailed Student's t-test for comparisons between two groups. One-way ANOVA with Tukey's multiple comparison test for

comparisons between multiple groups. P-values of significant results are presented in graph. Significance level $\alpha < 0.05$.

We then employed a different method to examine the presence of cytosolic and extracellular DNA following RSV infection. As previously performed by others (83, 89), we quantified the presence of DNA in the cytosol and extracellular milieu. DNA quantification was performed by conducting a qPCR for nDNA (*GAPDH* DNA) and mtDNA (*MT-ND1* and *MT-CO2*) in the cytosolic and extracellular fractions. nDNA and mtDNA were related to the presence of 18S DNA in the nuclear fraction, which was assumed to be stable across all samples. The results showed some inter-experiment variability, but with a tendency towards increased nDNA and mtDNA in the cytosol (Fig. 10a). Similarly to the cytosolic fraction, the content of mtDNA and nDNA showed a tendency towards increasing in the extracellular milieu (Fig. 10b). However, due to the large variations between the replicates, this experiment must be repeated to confirm these findings. All together, these results show that γH2AX, nDNA, and mtDNA are present in the cytoplasm after RSV infection. Additionally, these results suggest that nDNA and mtDNA are detectable in the extracellular milieu.

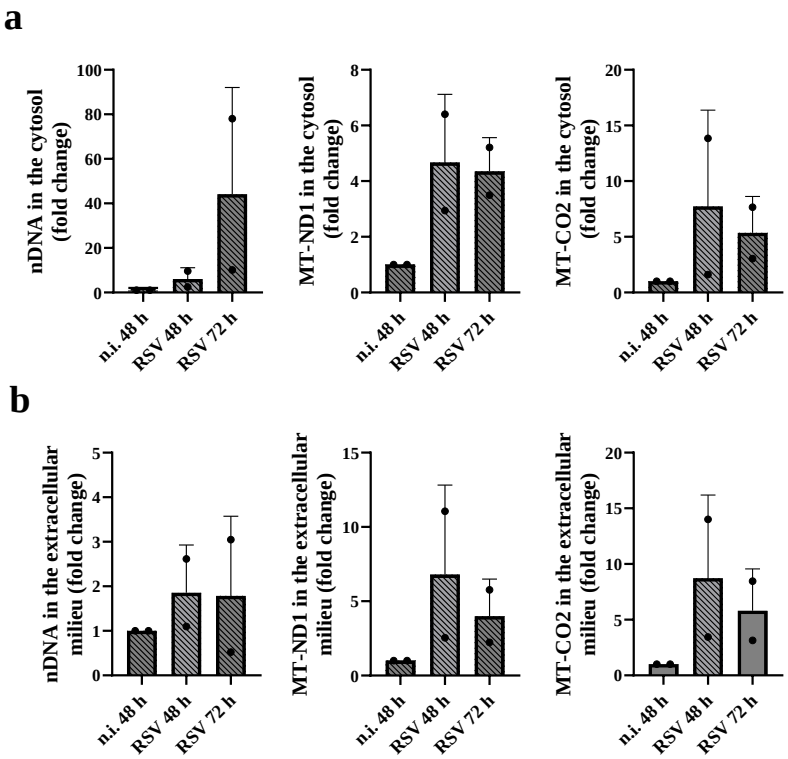


**Figure 10. Mitochondrial and nuclear DNA are detectable in the cytosol and extracellular milieu after RSV infection. (a, b)** Wi-38 cells were infected with RSV at a multiplicity of infection (MOI) of 3 for 48 and 72 h, before they were enriched into three fractions: cytosol, mitochondria, and nucleus. The levels of nuclear DNA

(nDNA) (*GAPDH* gDNA) and mitochondrial DNA (mtDNA) (*MT-ND1* and *MT-CO2*) in the cytosol and extracellular milieu were analyzed by qPCR with 18S DNA from the nuclear fraction as the endogenous control. nDNA and mtDNA in the two fractions are presented as fold changes relative to n.i. cells. The data are collected from two independent experiments. All quantitative results are presented as mean ± SD.

## 3.6 Low overall co-localization between cGAS, DAPI, and γH2AX in the cytoplasm

Since cGAS is activated by cytoplasmic DNA, it is important to determine the extent of co-localization between cGAS and DNA in the cytoplasm of RSV-infected cells (32). Additionally, cGAS has been shown to co-localize with γH2AX in the cytoplasm, which is associated with cGAS activation (70, 90). Thus, we sought to evaluate the extent of co-localization between cGAS, the DNA marker DAPI, and γH2AX within the cytoplasm of RSV-infected Wi-38 cells. The cytoplasm was defined as an area of 60 pixels surrounding the nucleus. We utilized Mander's method of co-localization to determine the degree of co-localization between the three fluorohores (86).

As demonstrated previously, both cGAS, DAPI, and γH2AX exhibit cytoplasmic localization after RSV infection. Notably, in Ex. 1, but not in Ex. 2 (Fig. 11a), weak extranuclear DAPI staining is evident, providing a visual representation of DNA within the cytoplasm. While visual indications of co-localization between cGAS, DAPI, and γH2AX are apparent (denoted by arrows in Fig. 11a), quantitative analysis revealed a limited degree of overall co-localization between all fluorophores (Fig. 11b). A higher proportion of DAPI localizes to cGAS (~0.22), compared to the fraction of cGAS localizing to DAPI (~0.05). Likewise, γH2AX co-localized with cGAS more frequently than cGAS with γH2AX (~0.26 and ~0.09, respectively). Interestingly, DAPI and γH2AX showed almost no co-localization in the cytoplasm (~0.02 and ~0.07). Together, these results indicate low overall co-localization between cGAS, DAPI, and γH2AX in the cytoplasm, suggesting a limited recruitment of cGAS to the sites of DNA and γH2AX. Due to co-localization analysis not being evidence for physical interaction, combined with time restraints, this experiment was not repeated. Negative controls for this experiment can be found in the appendix (appendix Fig. A2).

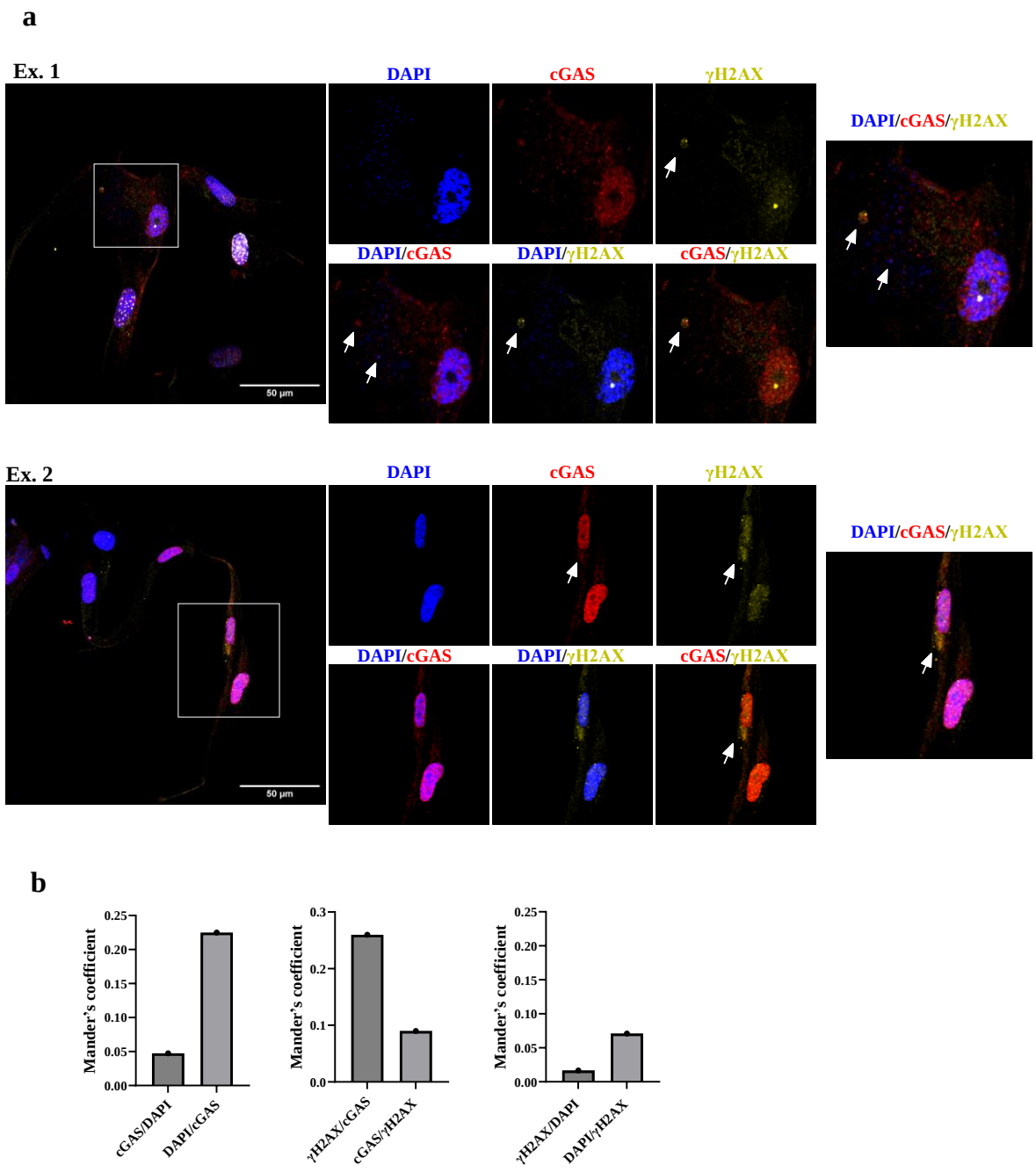


**Figure 11: Low degree of overall co-localization between cGAS, DAPI, and γH2AX in the cytoplasm**. **(a)** Two example images showing Wi-38 cells 48 h after RSV infection at a multiplicity of infection of 3. The cells were stained for DAPI, cGAS, and γH2AX, with arrows denoting regions with visual indications of co-localization. Cells were also stained with rabbit IgG and mouse IgG1 isotype controls as negative controls for cGAS and γH2AX, respectively (appendix. Fig. A2). **(b)** The degree of co-localization was quantified for all cells from one experiment (n=96) using Mander's method of co-localization with Costes' thresholding strategy and presented as a mean value of all measurements. The fluorophore first denoted represents the fraction of that fluorophore overlapping with the latter. e.g., cGAS/DAPI is the fraction of pixels staining positive for cGAS in the cytoplasm that are also positive for DAPI. In contrast, DAPI/cGAS is the fraction of pixels positive for DAPI that are also positive for cGAS.

## 3.7 RSV infection leads to decreased expression of structural proteins in the nuclear lamina

Previous work in SARS-CoV-2-infected cells showed that syncytia formation disrupts the cytoskeleton network, leading to the loss of integrity of the nuclear envelope and subsequent DNA leakage to the cytoplasm (69, 70). The underlying mechanism was decreased cytoskeletal stiffness, which lowered the amount of the nuclear lamina proteins lamin A/C. In addition, lamin B1 remains relatively constant upon mechanical changes but is degraded in senescent cells (66). We sought to determine if RSV infection affected the expression of lamin A/C and lamin B1. We cultured and infected cells with RSV at a MOI of 3 for various durations ranging from 24 to 72 h. After lysing the cells, the expression of lamin A/C and lamin B1 was determined by Western blotting and quantified in relation to the housekeeping gene GAPDH.

The results suggest a decrease in lamin B1 expression in RSV-infected cells at all timepoints and in diABZI-stimulated cells, compared to n.i. cells (Fig. 12a and b). Lamin A and C expression fell drastically between 24 h and 36 h post-infection and appeared unchanged after diABZI stimulation (Fig. 12c and d). Together, these results suggest a weakening of the nuclear envelope, potentially contributing to the cytoplasmic presence of nDNA. In addition, the decrease in lamin B1 expression could be indicative of the development of senescence in RSV-infected cells, potentially downstream of STING, as suggested by the diABZI-induced reduction of lamin B1.

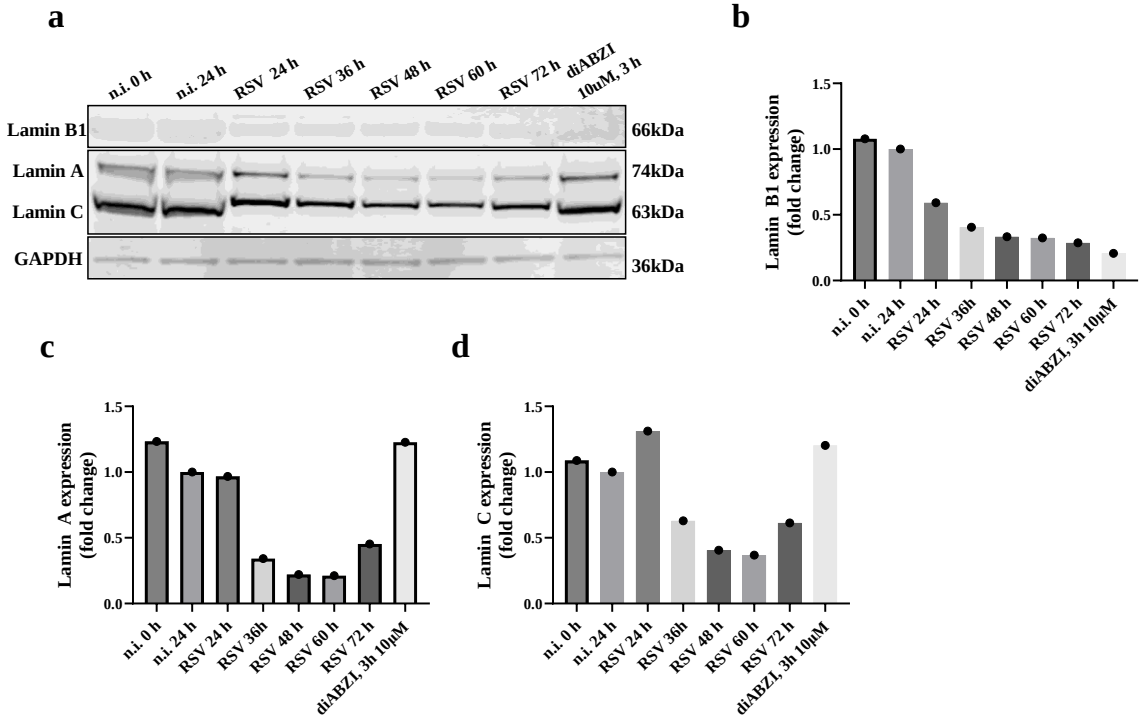


**Figure 12: Decreased expression of proteins from the nuclear lamina after RSV infection. (a)** Western blot depicting the expression levels of lamin B, lamin A/C, and the housekeeping gene GAPDH at various times following RSV infection at an MOI of 3. **(b-d)** The expression levels of lamin B and lamin A/C were normalized to GAPDH and are presented as fold change relative to non-infected (n.i.) cells after 24 h.

## 3.8 γH2AX and antiviral signaling components in the post-acute phase of RSV infection

An acute infection is characterized by the rapid onset of disease, which can be resolved by the host or end up killing the host (91). The presence of extracellular DNA in the lung has the potential to contribute to the immunopathology of RSV infection and can cause sterile inflammation after the acute infection (61-63). Therefore, it is of relevance to determine whether DNA damage and release persist in the post-acute phase of infection. To experimentally model the post-acute state, we infected Wi-38 cells with RSV at a MOI of 3 for 60 h before extensive washing to reduce extracellular virus. Cells were sampled at 0, 4, 8, 12, 24, 36, and 48 h post-washing (Fig. 13a). Protein expression was determined by Western blotting. The expression of γH2AX increased at all time points post-washing, compared to non-infected cells, but with large variations in the fold change between the three replicates (Fig. 13b and c). Additionally, cGAS expression and STING phosphorylation (Ser366) increased post-infection. A minor increase in phosphorylation of IRF3 (Ser396) was seen in post-RSV cells, which

returned to the levels of non-infected cells 48 h after washing (Fig. 13d). The phosphorylation of the NF-κB subunit P65 (Ser536) was similar to n.i. cells. STAT1 was markedly phospshorylated (Tyr107) in post-RSV cells, indicating an IFN response that decreased at later timepoints (Fig. 13e). After washing, the confluency of the cells remained steady for 24 h, before rapidly falling, indicating that washing slowed the progression of infection. However, the infection was not cleared within the time frame of the experiment, as evidenced by the increasing expression of $F_0$ throughout the experiment (Fig. 13f and g).

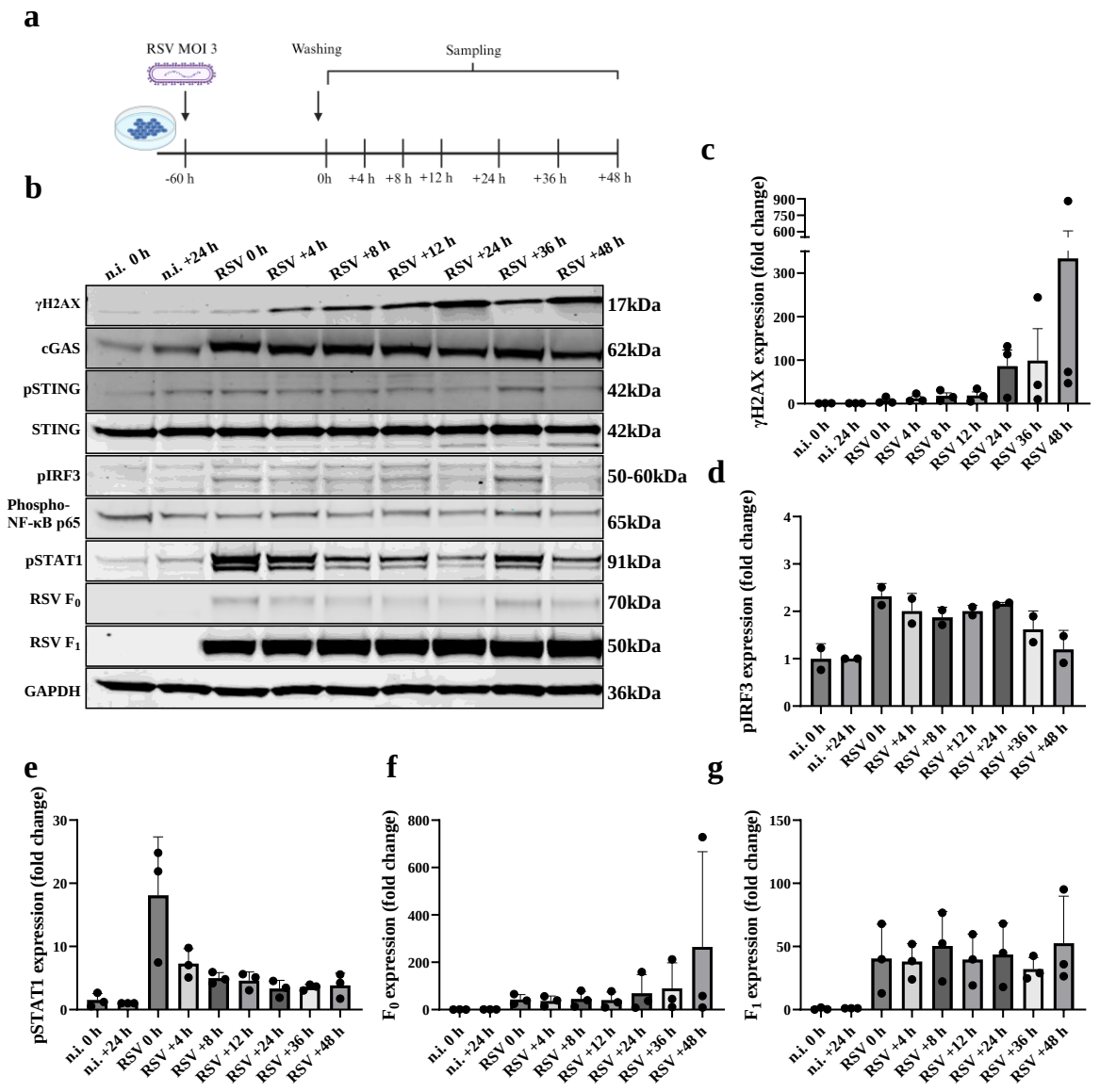


**Figure 13: γH2AX, innate immune components and RSV levels in a model of the post-acute phase of RSV infection. (a)** Wi-38 cells were infected with RSV at a multiplicity of infection of 3 for 60 h. After rigorous washing, cells were lysed after 0, 4, 8, 12, 24 and 48. **(b)** Protein expression levels were assessed by Western blotting. **(c-g)** Protein levels from three biological replicates were quantified and are presented as fold change

compared to n.i. +24 h. One replicate of pIRF3 was excluded due to a technical error. All quantitative results are presented as mean ± SD.

To assess the release of DNA into the extracellular milieu, DNA was isolated from the growth medium and whole-cell extracts before analysis of nDNA and mtDNA by qPCR. While significant variability between replicates was observed, there were signs of a rise in nDNA and mtDNA levels rapidly after washing, which remained above the levels observed in n.i. cells throughout the experiment (Fig. 14 a-c). Altogether, these results suggest that RSV infection leads to persistent DNA damage and leakage of DNA to the extracellular space *in vitro,* along with sustained immune activation indicated by increased expression of cGAS and STING phosphorylation. Decreasing STAT1 phosphorylation might indicate a diminishing IFN response, despite increasing viral replication at later time points.

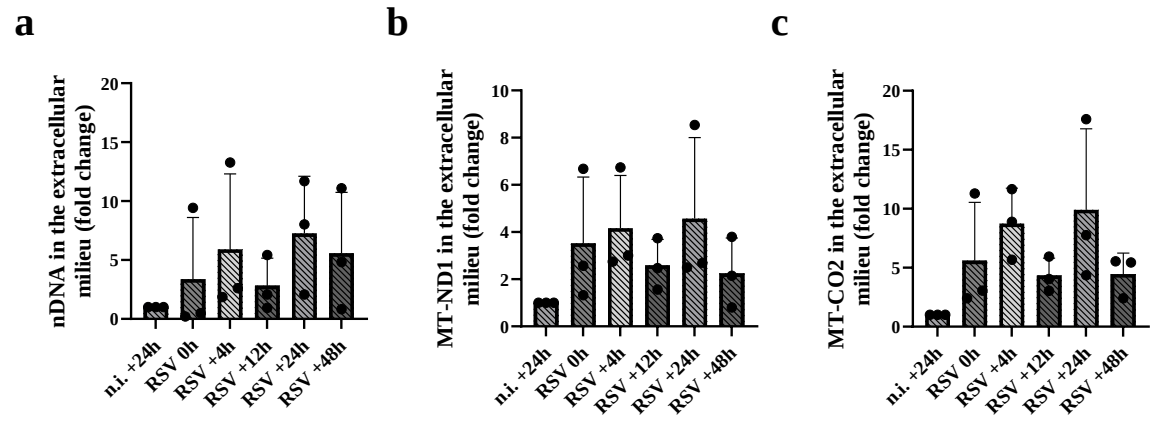


**Figure 14: Nuclear and mitochondrial DNA in the extracellular milieu in a model of the post-acute phase of RSV infection. (a-c)** Wi-38 cells were infected with RSV at a multiplicity of infection of 3 for 60 h. After rigorous washing, cells were harvested and the growth medium was collected for DNA isolation at 0, 4, 8, 12, 24 and 48 h post washing. The content of nuclear DNA (GAPDH gDNA) and mitochondrial DNA (*MT-ND1* and *MT-CO2*) in the extracellular milieu was studied using qPCR. DNA from the extracellular milieu was related to DNA from whole cell extracts (18S DNA) and is expressed as fold change compared to n.i. +24 h. All quantitative results are presented as mean ± SD.

# 4. Discussion

The cGAS-STING pathway plays a central role in the detection of DNA viruses. However, knowledge about cGAS-STING in the antiviral response against RNA viruses is scarce, and its implication in RSV infection is currently unexplored. In this thesis, we sought to determine the subcellular localization of cGAS in uninfected and RSV-infected Wi-38 cells. Moreover, we explored whether RSV infection causes DNA damage and leakage of nDNA and mtDNA into the cytoplasm and supernatant of RSV-infected cells. Furthermore, we made a first leap to describe the kinetics of DNA damage and immune signaling in the post-acute phase of RSV infection.

## 4.1 Proposed mechanism of cGAS activation after RSV infection.

Based on the results obtained in this thesis and previous research, we propose a mechanism for cGAS-STING activation following RSV infection in Wi-38 cells. We propose that syncytia formation leads to disruption of the cytoskeletal network. This mechanical damage, potentially in combination with RSV-induced ROS production, reduce the integrity of the nuclear envelope, the mitochondrial membrane, and the plasma membrane, thereby causing cytoplasmic and extracellular release of DNA (Fig. 15a). As a response to cytoplasmic DNA, cGAS translocates from the nucleus to the cytoplasm, where it senses dsDNA and produces cGAMP. cGAMP activates STING signaling through the canonical cGAS-STING pathway (Fig. 15b).

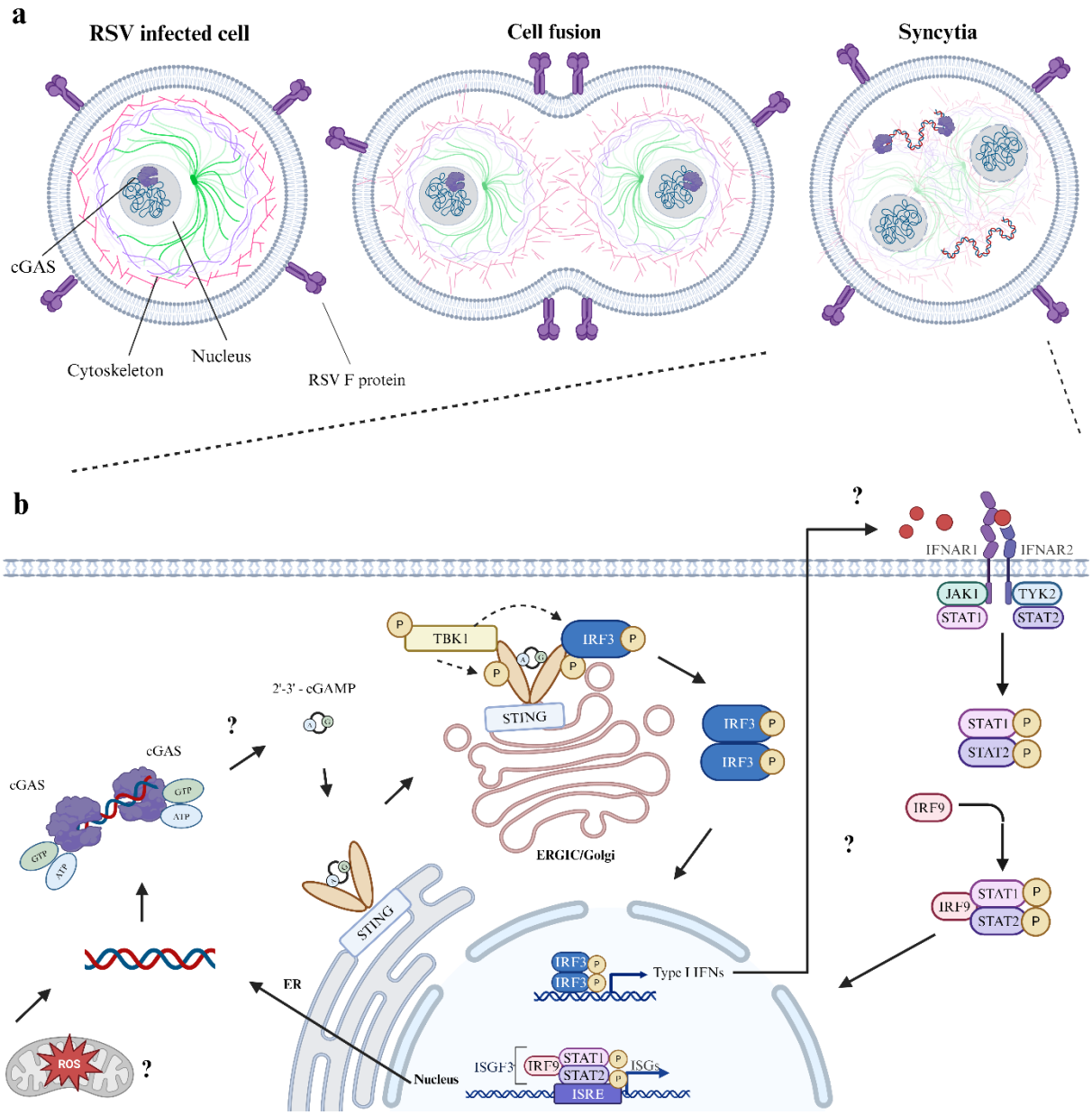


**Figure 15: Proposed mechanism of cGAS activation following RSV activation. (a)** cGAS is localized to the nucleus in uninfected cells. RSV-infected cells express the RSV F protein on the surface, which causes fusion of adjacent cells and the formation of syncytia. During this process, the cytoskeleton collapses, leading to the loss of integrity of the nuclear envelope and subsequent nDNA leakage into the cytoplasm. **(b)** mtDNA is also present in the cytoplasm, potentially due to ROS production. In the cytoplasm, cGAS binds DNA and produces cGAMP, which activates STING in a canonical manner, leading to IFN and ISG production. Question marks denote non-investigated steps. The figure was created with BioRender (www.biorender.com).

## 4.2 cGAS is present in the nucleus of noninfected Wi-38 cells, while also being present in the cytoplasm after RSV infection

cGAS has both NLSs and a NES, which indicates that both cytoplasmic and nuclear presence is possible. However, the subcellular localization of cGAS in the lung fibroblasts, Wi-38, has never been studied (44, 47). We report that cGAS is detectable only in the nucleus of non-infected Wi-38 cells, while also being localized to the cytoplasm upon infection with RSV, an RNA virus.

Previous research has reported varying patterns of cGAS localization in fibroblasts. For instance, cGAS was reported to be primarily a nuclear protein in the mouse fibroblast cell line L929 while being evenly distributed between the nucleus and cytoplasm in some primary fibroblasts, as well as in the human fibroblast cell lines HFF and HCA2-TERT. (42, 45, 92). In contrast, cGAS has been found almost exclusively in the cytoplasm of some primary fibroblasts, suggesting that nuclear localization is not a universal characteristic across all fibroblasts (45). Thus, cGAS localization might be influenced by unknown cell-specific factors as well as infections and the instance of mislocated DNA (42, 93).

Interestingly, our results demonstrate that cGAS translocates to the cytoplasm of Wi-38 cells upon RSV infection. Cytoplasmic translocation of cGAS has been described in HeLa cells after DNA stimulation but was blocked by inhibition of the exportin protein CRM1, indicating that cGAS is actively transported across the nuclear envelope (47). It is worth mentioning that active cGAS translocation has not previously been described following infection with an RNA virus. However, cGAS has been shown to bind tightly to γH2AX (45, 48), and our results show that γH2AX and DNA are present in the cytoplasm after RSV infection, suggesting that structural damage could contribute to the cytoplasmic translocation of cGAS. Whether cytoplasmic cGAS translocation after RSV infection is due to active transport and/or a side effect of damage to the nuclear envelope is a question for future research. Exploring the temporal induction of DSBs and cGAS translocation would facilitate the understanding of the underlying mechanisms. Establishment of the correct titers of rgRSV, the fluorescently tagged RSV, would allow for real-time tracking of infection and would be invaluable for studying temporal changes in cGAS localization and DSB induction.

## 4.3 RSV infection induces DNA damage and DNA leakage to the cytosol and extracellular space

One study from 2016 reported that RSV infection caused DNA damage (73). We strengthen these findings by showing a strong induction of γH2AX following RSV infection, indicative of DSBs. In addition, we detect nDNA and mtDNA in the cytoplasm after RSV infection, potentially serving as ligands for cytoplasmic DNA sensors. The observation that cGAS translocates to the cytoplasm might suggest that the cGAS-STING axis is an important response mechanism to the presence of cytoplasmic DNA.

SARS-CoV-2 infection was reported to cause DNA damage and DNA release to the cytoplasm due to the formation of syncytia, which disrupts the cytoskeleton network, leading to lost nuclear integrity and micronuclei formation (69, 70). As RSV is known to cause syncytia, lost structural integrity offers an appealing hypothesis about the mechanism of extranuclear and extracellular nDNA leakage. In one experiment, we found a time-dependent decrease in lamin A/C expression after RSV infection (Fig. 12), suggesting a weakening of the nuclear envelope due to mechanical damage, possibly caused by syncytia formation. Moreover, lamin A/C can be phosphorylated downstream of DNA damage, which hinders its assembly and thereby further weakens the nuclear envelope (94).

Expression of Lamin B1 was reported to remain constant during SARS-CoV-2 infection (70). In contrast, we detected a decrease in lamin B1 expression after RSV infection. Since, lamin B1 is known to be stably expressed upon mechanical damage, a decrease in lamin B1 levels indicates that factors besides mechanical damage also plays a role in the weakening of the nuclear envelope (95). Lamin B degradation is one of the hallmarks of senescence, which causes micronuclei formation and inflammation (66). Thus, lamin B1 degradation could indicate that RSV-infected Wi-38 cells enter senescence, as previously described for A549 cells (73). Moreover, we found that lamin B expression, but not lamin A/C expression, was decreased in diABZI-stimulated cells. This suggests that senescence could be triggered downstream of STING, potentially via the non-canonical STING-PERK-eIF2α pathway, which has demonstrated the ability to induce senescence in a cGAS-dependent manner (56). As these results are only based on one experiment, future research should aim to confirm these findings and expand on the potential link between RSV infection and senescence.

Our findings also revealed an elevation of mtDNA in both the cytosol and extracellular space following RSV infection. There is a known association between mitochondrial function and the

cytoskeletal network, suggesting that structural disruption could lead to mtDNA release (96). Furthermore, ROS may play a role in promoting the extracellular release of nDNA and mtDNA by influencing the integrity of the plasma membrane (97). RSV infection has been demonstrated to increase the production of mitochondrial ROS, and this was highlighted as the primary cause of DSBs in nDNA in RSV-infected A549 cells (73, 98). Moreover, ROS-induced mtDNA release serves to activate cGAS (68). Together, ROS production is likely to play a role in both the DNA damage and subsequent DNA release from the mitochondria and nucleus observed after RSV infection.

Overall, the mechanisms leading to DNA damage and nDNA and mtDNA release after RSV infection in Wi-38 cells are poorly understood. Our findings suggest that DNA damage and DNA release from the nucleus and mitochondria are, at least partially, driven by a loss of structural integrity of the nuclear envelope following RSV infection. However, based on previous research, it is likely that mitochondrial ROS production is involved in both DNA damage and DNA release to the cytosol and extracellular space in RSV-infected cells. Of note, although not investigated here, we cannot rule out the possibility that DSBs and DNA leakage are caused by direct viral activity rather than secondary effects such as syncytia formation and ROS production.

## 4.4 Self DNA as a ligand for cGAS

cGAS has previously been found to partially co-localize with both the DNA probe DAPI and γH2AX in the cytoplasm of cells after micronuclei budding, which facilitated its activation (70, 90). In this thesis, we used Mander's method of co-localization to assess the degree of overlapping fluorescent signals between cGAS, DAPI, and γH2AX in the cytoplasm of RSV-infected cells (86). Our results indicate a weak overlap between the three fluorophores, suggesting that cGAS is not actively recruited to the sites of DAPI and γH2AX in the cytoplasm.

cGAS has been shown to stimulate autophagy of cytosolic DNA, suggesting that cGAS-bound DNA is only transiently present in the cytoplasm, thereby influencing the overall co-localization of cGAS with DAPI or γH2AX (99, 100). Moreover, an infection period of 48 h was used in our experiment, while the strongest STING phosphorylation in Wi-38 cells seemed to be 60 h after infection (Fig. 5), indicating that later inspection could have yielded stronger overall co-localization. Interestingly, the low level of co-localization between DAPI and γH2AX suggests that γH2AX dissociates from DNA after release to the cytoplasm and/or that γH2AX is retained

in the cytoplasm after DNA degradation. It is important to note, however, that significant portions of the DNA in the cytoplasm might fall outside the limit of detection due to the weak fluorescence intensity obtained from DAPI staining, potentially affecting the results (101).

Overall, even though our results show limited co-localization between cGAS, DAPI, and γH2AX in the cytoplasm, it is important to note that co-localization analysis does not provide evidence of physical interaction (102). Additionally, the limited degree of co-localization between cGAS, DAPI, and γH2AX, might indeed be sufficient to cause the activation of cGAS. Our data support cGAS activation by demonstrating STING phosphorylation, which has only been shown downstream of cGAMP production. As these results are representative of one experiment, future research should aim to re-evaluate these findings. In conclusion, direct evidence of cGAS-DNA interaction via chromatin immunoprecipitation alongside measurements of cGAMP would help validate the hypothesis that self-DNA activates cGAS following RSV infection.

## 4.5 Post-acute phase of RSV infection

To our knowledge, we made the first attempt at categorizing the kinetics of DNA damage and immune signaling in the post-acute phase of RSV infection. Exploration of the post-acute phase of RSV infection is promising for unraveling whether RSV-induced genomic instability endures over the long term. Such investigation may shed light on potential mechanisms underlying sterile inflammation, COPD, and pulmonary fibrosis following RSV infection. We showed that removal of the viral growth medium and extensive washing halted the progression of infection for 24 hours, thereby mimicking the post-acute phase of RSV infection. The slowed progression of infection was evidenced by the stabilization of cell confluency and the expression of the viral proteins $F_0$ and $F_1$. Despite the reduction in viral load, the expression of γH2AX continued to increase post-washing, while nDNA and mtDNA were released extracellularly.

Previous research has demonstrated that the expression of γH2AX correlates temporarily with the induction and repair of DSBs (103, 104). Thus, our results indicate a continuous increase in DSBs, despite a reduction in the viral load. The miscorrelation between actively infecting viruses and DSB induction supports our hypothesis that DNA damage is caused by secondary mechanisms like syncytia formation and ROS production rather than direct viral activity. Cells that were infected with RSV pre-washing would still display the F-protein on the surface and be capable of fusing with adjacent cells. Likewise, and possibly even more potent, could be the

probable ROS production after infection. The number of γH2AX foci has been shown to be drastically reduced upon antioxidative treatment of RSV-infected cells (73). Thus, a continuous increase in γH2AX expression suggests ongoing ROS production and possibly deficient ROS clearance. Furthermore, DNA damage has been observed in mice long after the clearance of the virus. The DNA damage was associated with the induction of senescence, suggesting that RSV can induce persistent alteration in the target cells (73). As senescent cells have higher ROS production due to alterations in metabolism and reduced capacity to regenerate, RSV-induced senescence displays a tempting explanation for the increase of γH2AX in our model of the post-acute phase of infection (105, 106).

We have shown that both nDNA and mtDNA are released extracellularly in our model of the post-acute phase of RSV infection. The post-acute, extracellular release of DNA has the potential to contribute to sterile inflammation, making these findings relevant for the long-term pathogenesis of RSV infection (61-63). The release of extracellular DNA may be attributed to syncytia formation and ROS production. In addition, RSV-infected cells have been shown to undergo necroptosis and pyoptosis, allowing for the efflux of cellular content like DNA into the extracellular space. This lytic form of cell death would likely proceed in our post-acute model of RSV infection (107-109). The observation that nDNA and mtDNA remain at a relatively constant but elevated level in the supernatant might indicate that DNA release ceases or that free DNA is degraded upon release.

Finally, it is worth noting the continuous decline in STAT1 phosphorylation, despite a slightly elevated and stable phospho-IRF3 expression in post-RSV cells. The reduction in phosphorylated STAT1 suggests a diminishing IFN response, regardless of the increasing expression of the RSV $F_0$ protein observed from 24 hours post-washing. The inverse relationship between $F_0$ expression and STAT1 phosphorylation could be attributed to immune evasion downstream of IRF3. RSV has previously been demonstrated to interfere with Tyk2, thereby hindering the phosphorylation of STAT1, highlighting a potential mechanism (110). Another possibility is the desensitization of IFNAR. Transient IFN-γ exposure has been shown to induce a negative feedback loop, resulting in rapid dephosphorylation of STAT1 upon re-exposure to IFN-γ, thereby attenuating STAT1 (111). Likewise, transient exposure to type I IFNs might potentially cause desensitization of IFNAR. Future research could investigate the kinetics of type I IFN signaling in the post-acute phase of RSV infection.

# 5. Conclusion

This thesis aimed to investigate the sub-cellular localization of cGAS in Wi-38 cells and the potential presence of DNA in the cytoplasm and extracellular space after infection by RSV. Our results revealed that cGAS was predominantly located in the nucleus of Wi-38 cells. Furthermore, we demonstrated that cGAS translocated from the nucleus to the cytoplasm after RSV infection, accompanied by an increased cytosolic presence of both nDNA and mtDNA. We show that RSV infection increased the number of γH2AX foci, indicative of double strand breaks in nDNA. Additionally, our results suggest extracellular release of DNA. Despite the presence of cGAS and DNA in the cytoplasm, our analysis showed low overall co-localization. Finally, we made the first attempt at describing the kinetics of DNA damage in the post-acute phase of RSV infection, where we demonstrated a continuous increase in DSBs despite a reduction in viral load.

We propose a mechanism wherein syncytia formation, possibly supported by ROS production, induces cellular damage, resulting in the breakdown of DNA compartmentalization. We suggest that self-DNA in the cytosol, both of nuclear and mitochondrial origin, activates the cGAS-STING immune axis. Additionally, we highlight potential connections between the induction of DNA damage and senescence following RSV infection, which could be a topic of future research. This thesis illustrates the involvement of the cGAS-STING pathway in the antiviral response to RSV, offering deeper insights into the mechanisms of innate immunity against RNA viruses. Understanding how RNA viruses can trigger DNA damage and activate innate immune signaling pathways could pave the way for the development of novel targeted therapeutic strategies against viral infections.

# References

1. Denny FW, Jr. The clinical impact of human respiratory virus infections. Am J Respir Crit Care Med. 1995;152(4 Pt 2):S4-12.
2. Chonmaitree T, Revai K, Grady JJ, Clos A, Patel JA, Nair S, et al. Viral upper respiratory tract infection and otitis media complication in young children. Clin Infect Dis. 2008;46(6):815-23.
3. Fendrick AM, Monto AS, Nightengale B, Sarnes M. The economic burden of non-influenza-related viral respiratory tract infection in the United States. Arch Intern Med. 2003;163(4):487-94.
4. Matteelli A, Saleri N, Ryan ET. Respiratory Infections. Travel Medicine. 2013:511-22.
5. Grief SN. Upper respiratory infections. Prim Care. 2013;40(3):757-70.
6. Dasaraju PV, Liu C. Infections of the Respiratory System. In: Baron S, editor. Medical Microbiology. Galveston (TX): University of Texas Medical Branch at Galveston



7. Wu D, Wu T, Liu Q, Yang Z. The SARS-CoV-2 outbreak: What we know. Int J Infect Dis. 2020;94:44-8.
8. Baraldi E, Checcucci Lisi G, Costantino C, Heinrichs JH, Manzoni P, Riccò M, et al. RSV disease in infants and young children: Can we see a brighter future? Hum Vaccin Immunother. 2022;18(4):2079322.
9. Chanock R, Roizman B, Myers R. Recovery from infants with respiratory illness of a virus related to chimpanzee coryza agent (CCA). I. Isolation, properties and characterization. Am J Hyg. 1957;66(3):281-90.
10. Glezen WP, Taber LH, Frank AL, Kasel JA. Risk of primary infection and reinfection with respiratory syncytial virus. Am J Dis Child. 1986;140(6):543-6.
11. Shi T, McAllister DA, O'Brien KL, Simoes EAF, Madhi SA, Gessner BD, et al. Global, regional, and national disease burden estimates of acute lower respiratory infections due to respiratory syncytial virus in young children in 2015: a systematic review and modelling study. Lancet. 2017;390(10098):946-58.
12. Haber N. Respiratory syncytial virus infection in elderly adults. Med Mal Infect. 2018;48(6):377-82.
13. Baraldi F, Contoli M, Papi A. The Convoluted Journey to Unveil the Respiratory Syncytial Virus (RSV) in Chronic Obstructive Pulmonary Disease (COPD) Exacerbations: Old Paths and New Traces. Am J Respir Crit Care Med. 2024.
14. Sikkel MB, Quint JK, Mallia P, Wedzicha JA, Johnston SL. Respiratory Syncytial Virus Persistence in Chronic Obstructive Pulmonary Disease. The Pediatric Infectious Disease Journal. 2008;27(10).
15. Savin IA, Zenkova MA, Sen'kova AV. Pulmonary Fibrosis as a Result of Acute Lung Inflammation: Molecular Mechanisms, Relevant In Vivo Models, Prognostic and Therapeutic Approaches. Int J Mol Sci. 2022;23(23).
16. Topalidou X, Kalergis AM, Papazisis G. Respiratory Syncytial Virus Vaccines: A Review of the Candidates and the Approved Vaccines. Pathogens. 2023;12(10).

17. Wright M, Piedimonte G. Respiratory syncytial virus prevention and therapy: past, present, and future. Pediatr Pulmonol. 2011;46(4):324-47.
18. Borchers AT, Chang C, Gershwin ME, Gershwin LJ. Respiratory syncytial virus--a comprehensive review. Clin Rev Allergy Immunol. 2013;45(3):331-79.
19. McLellan JS, Ray WC, Peeples ME. Structure and function of respiratory syncytial virus surface glycoproteins. Curr Top Microbiol Immunol. 2013;372:83-104.
20. Battles MB, McLellan JS. Respiratory syncytial virus entry and how to block it. Nature Reviews Microbiology. 2019;17(4):233-45.
21. Collins PL, Fearns R, Graham BS. Respiratory syncytial virus: virology, reverse genetics, and pathogenesis of disease. Curr Top Microbiol Immunol. 2013;372:3-38.
22. Gould PS, Easton AJ. Coupled translation of the second open reading frame of M2 mRNA is sequence dependent and differs significantly within the subfamily Pneumovirinae. J Virol. 2007;81(16):8488-96.
23. Reeves SR, Barrow KA, Rich LM, White MP, Shubin NJ, Chan CK, et al. Respiratory Syncytial Virus Infection of Human Lung Fibroblasts Induces a Hyaluronan-Enriched Extracellular Matrix That Binds Mast Cells and Enhances Expression of Mast Cell Proteases. Front Immunol. 2019;10:3159.
24. Johnson JE, Gonzales RA, Olson SJ, Wright PF, Graham BS. The histopathology of fatal untreated human respiratory syncytial virus infection. Modern Pathology. 2007;20(1):108-19.
25. Tayyari F, Marchant D, Moraes TJ, Duan W, Mastrangelo P, Hegele RG. Identification of nucleolin as a cellular receptor for human respiratory syncytial virus. Nature Medicine. 2011;17(9):1132-5.
26. Mastrangelo P, Norris MJ, Duan W, Barrett EG, Moraes TJ, Hegele RG. Targeting Host Cell Surface Nucleolin for RSV Therapy: Challenges and Opportunities. Vaccines (Basel). 2017;5(3).
27. Ghildyal R, Ho A, Jans DA. Central role of the respiratory syncytial virus matrix protein in infection. FEMS Microbiol Rev. 2006;30(5):692-705.
28. Gagliardi TB, Criado MF, Proença-Módena JL, Saranzo AM, Iwamoto MA, de Paula FE, et al. Syncytia Induction by Clinical Isolates of Human Respiratory Syncytial Virus A. Intervirology. 2017;60(1-2):56-60.
29. Tian J, Huang K, Krishnan S, Svabek C, Rowe DC, Brewah Y, et al. RAGE inhibits human respiratory syncytial virus syncytium formation by interfering with F-protein function. J Gen Virol. 2013;94(Pt 8):1691-700.
30. Thompson MR, Kaminski JJ, Kurt-Jones EA, Fitzgerald KA. Pattern recognition receptors and the innate immune response to viral infection. Viruses. 2011;3(6):920-40.
31. Takeuchi O, Akira S. Pattern Recognition Receptors and Inflammation. Cell. 2010;140(6):805-20.
32. Chen C, Xu P. Cellular functions of cGAS-STING signaling. Trends in Cell Biology. 2023;33(8):630-48.
33. Mesev EV, LeDesma RA, Ploss A. Decoding type I and III interferon signalling during viral infection. Nature Microbiology. 2019;4(6):914-24.
34. Schneider WM, Chevillotte MD, Rice CM. Interferon-stimulated genes: a complex web of host defenses. Annu Rev Immunol. 2014;32:513-45.

35. Carty M, Guy C, Bowie AG. Detection of Viral Infections by Innate Immunity. Biochemical Pharmacology. 2021;183:114316.
36. Zeng R, Cui Y, Hai Y, Liu Y. Pattern recognition receptors for respiratory syncytial virus infection and design of vaccines. Virus Research. 2012;167(2):138-45.
37. Mifsud EJ, Kuba M, Barr IG. Innate Immune Responses to Influenza Virus Infections in the Upper Respiratory Tract. Viruses. 2021;13(10).
38. Karki R, Kanneganti T-D. Innate immunity, cytokine storm, and inflammatory cell death in COVID-19. Journal of Translational Medicine. 2022;20(1):542.
39. Van Royen T, Rossey I, Sedeyn K, Schepens B, Saelens X. How RSV Proteins Join Forces to Overcome the Host Innate Immune Response. Viruses. 2022;14(2).
40. Ivashkiv LB, Donlin LT. Regulation of type I interferon responses. Nature Reviews Immunology. 2014;14(1):36-49.
41. Chen Q, Sun L, Chen ZJ. Regulation and function of the cGAS–STING pathway of cytosolic DNA sensing. Nature Immunology. 2016;17(10):1142-9.
42. Barnett KC, Coronas-Serna JM, Zhou W, Ernandes MJ, Cao A, Kranzusch PJ, Kagan JC. Phosphoinositide Interactions Position cGAS at the Plasma Membrane to Ensure Efficient Distinction between Self- and Viral DNA. Cell. 2019;176(6):1432-46.e11.
43. Qiu S, Zhong X, Meng X, Li S, Qian X, Lu H, et al. Mitochondria-localized cGAS suppresses ferroptosis to promote cancer progression. Cell Research. 2023;33(4):299-311.
44. Kim EY, Basit A, Kim WJ, Ko EB, Lee JH. Multi-functional regulation of cGAS by the nuclear localization signal2 (NLS2) motif: Nuclear localization, enzyme activity and protein degradation. Biochem Biophys Res Commun. 2023;673:1-8.
45. Liu H, Zhang H, Wu X, Ma D, Wu J, Wang L, et al. Nuclear cGAS suppresses DNA repair and promotes tumorigenesis. Nature. 2018;563(7729):131-6.
46. Liu H, Wang F, Cao Y, Dang Y, Ge B. The multifaceted functions of cGAS. Journal of Molecular Cell Biology. 2022;14(5):mjac031.
47. Sun H, Huang Y, Mei S, Xu F, Liu X, Zhao F, et al. A Nuclear Export Signal Is Required for cGAS to Sense Cytosolic DNA. Cell Rep. 2021;34(1):108586.
48. Jiang H, Xue X, Panda S, Kawale A, Hooy RM, Liang F, et al. Chromatin-bound cGAS is an inhibitor of DNA repair and hence accelerates genome destabilization and cell death. Embo j. 2019;38(21):e102718.
49. Gekara NO, Jiang H. The innate immune DNA sensor cGAS: A membrane, cytosolic, or nuclear protein? Sci Signal. 2019;12(581).
50. Lahaye X, Gentili M, Silvin A, Conrad C, Picard L, Jouve M, et al. NONO Detects the Nuclear HIV Capsid to Promote cGAS-Mediated Innate Immune Activation. Cell. 2018;175(2):488-501.e22.
51. Chen H, Chen H, Zhang J, Wang Y, Simoneau A, Yang H, et al. cGAS suppresses genomic instability as a decelerator of replication forks. Sci Adv. 2020;6(42).
52. Zhao B, Xu P, Rowlett CM, Jing T, Shinde O, Lei Y, et al. The molecular basis of tight nuclear tethering and inactivation of cGAS. Nature. 2020;587(7835):673-7.
53. Malik P, Korfali N, Srsen V, Lazou V, Batrakou DG, Zuleger N, et al. Cell-specific and lamin-dependent targeting of novel transmembrane proteins in the nuclear envelope. Cellular and Molecular Life Sciences. 2010;67(8):1353-69.

54. Cheradame L, Guerrera IC, Gaston J, Schmitt A, Jung V, Goudin N, et al. STING protects breast cancer cells from intrinsic and genotoxic-induced DNA instability via a non-canonical, cell-autonomous pathway. Oncogene. 2021;40(49):6627-40.
55. Dixon CR, Malik P, de las Heras JI, Saiz-Ros N, de Lima Alves F, Tingey M, et al. STING nuclear partners contribute to innate immune signaling responses. iScience. 2021;24(9):103055.
56. Zhang D, Liu Y, Zhu Y, Zhang Q, Guan H, Liu S, et al. A non-canonical cGAS–STING–PERK pathway facilitates the translational program critical for senescence and organ fibrosis. Nature Cell Biology. 2022;24(5):766-82.
57. Zhang R, Kang R, Tang D. STING1 in Different Organelles: Location Dictates Function. Front Immunol. 2022;13:842489.
58. Nazmi A, Mukhopadhyay R, Dutta K, Basu A. STING Mediates Neuronal Innate Immune Response Following Japanese Encephalitis Virus Infection. Scientific Reports. 2012;2(1):347.
59. Hopfner K-P, Hornung V. Molecular mechanisms and cellular functions of cGAS–STING signalling. Nature Reviews Molecular Cell Biology. 2020;21(9):501-21.
60. Ablasser A, Chen ZJ. cGAS in action: Expanding roles in immunity and inflammation. Science. 2019;363(6431).
61. Cortjens B, de Boer OJ, de Jong R, Antonis AF, Sabogal Piñeros YS, Lutter R, et al. Neutrophil extracellular traps cause airway obstruction during respiratory syncytial virus disease. J Pathol. 2016;238(3):401-11.
62. Chen GY, Nuñez G. Sterile inflammation: sensing and reacting to damage. Nature Reviews Immunology. 2010;10(12):826-37.
63. Carignon S, De Moura Rodrigues D, Gosset D, Culerier E, Huot-Marchand S, Savigny F, et al. Lung inflammation and interstitial fibrosis by targeted alveolar epithelial type I cell death. Front Immunol. 2023;14:1261483.
64. Motwani M, Pawaria S, Bernier J, Moses S, Henry K, Fang T, et al. Hierarchy of clinical manifestations in SAVI N153S and V154M mouse models. Proc Natl Acad Sci U S A. 2019;116(16):7941-50.
65. Hatch EM, Fischer AH, Deerinck TJ, Hetzer MW. Catastrophic nuclear envelope collapse in cancer cell micronuclei. Cell. 2013;154(1):47-60.
66. Glück S, Guey B, Gulen MF, Wolter K, Kang T-W, Schmacke Niklas A, et al. Innate immune sensing of cytosolic chromatin fragments through cGAS promotes senescence. Nature Cell Biology. 2017;19(9):1061-70.
67. Lan YY, Heather JM, Eisenhaure T, Garris CS, Lieb D, Raychowdhury R, Hacohen N. Extranuclear DNA accumulates in aged cells and contributes to senescence and inflammation. Aging Cell. 2019;18(2):e12901.
68. Kim J, Kim H-S, Chung JH. Molecular mechanisms of mitochondrial DNA release and activation of the cGAS-STING pathway. Experimental & Molecular Medicine. 2023;55(3):510-9.
69. Ren H, Ma C, Peng H, Zhang B, Zhou L, Su Y, et al. Micronucleus production, activation of DNA damage response and cGAS-STING signaling in syncytia induced by SARS-CoV-2 infection. Biol Direct. 2021;16(1):20.

70. Zhou Z, Zhang X, Lei X, Xiao X, Jiao T, Ma R, et al. Sensing of cytoplasmic chromatin by cGAS activates innate immune response in SARS-CoV-2 infection. Signal Transduction and Targeted Therapy. 2021;6(1):382.
71. Jahun AS, Sorgeloos F, Chaudhry Y, Arthur SE, Hosmillo M, Georgana I, et al. Leaked genomic and mitochondrial DNA contribute to the host response to noroviruses in a STING-dependent manner. Cell Reports. 2023;42(3):112179.
72. Sun B, Sundström KB, Chew JJ, Bist P, Gan ES, Tan HC, et al. Dengue virus activates cGAS through the release of mitochondrial DNA. Scientific Reports. 2017;7(1):3594.
73. Martínez I, García-Carpizo V, Guijarro T, García-Gomez A, Navarro D, Aranda A, Zambrano A. Induction of DNA double-strand breaks and cellular senescence by human respiratory syncytial virus. Virulence. 2016;7(4):427-42.
74. Wu J, Sun L, Chen X, Du F, Shi H, Chen C, Chen ZJ. Cyclic GMP-AMP is an endogenous second messenger in innate immune signaling by cytosolic DNA. Science. 2013;339(6121):826-30.
75. Sun L, Wu J, Du F, Chen X, Chen ZJ. Cyclic GMP-AMP synthase is a cytosolic DNA sensor that activates the type I interferon pathway. Science. 2013;339(6121):786-91.
76. Estabillo L. Role of the cGAS-STING immune Axis and the Metabolic Regulator ATP Citrate Lyase in Respiratory Syncytial Virus Infection Trondheim: Norwegian University of Science and Technology; 2023.
77. M H. Exploring the cGAS-STING pathway and two fibrotic genes during respiratory syncytial virus infection. Trondheim: Norwegian university of Science and Technology; 2023.
78. Damlien E. Exploring the cGAS-STING immune pathway in infection with respiratory syncytial virus. Trondheim: Norwegian University of Science and Technology; 2023.
79. Ramanjulu JM, Pesiridis GS, Yang J, Concha N, Singhaus R, Zhang S-Y, et al. Design of amidobenzimidazole STING receptor agonists with systemic activity. Nature. 2018;564(7736):439-43.
80. Zhang L, Peeples Mark E, Boucher Richard C, Collins Peter L, Pickles Raymond J. Respiratory Syncytial Virus Infection of Human Airway Epithelial Cells Is Polarized, Specific to Ciliated Cells, and without Obvious Cytopathology. Journal of Virology. 2002;76(11):5654-66.
81. Wyatt LS, Moss B, Rozenblatt S. Replication-deficient vaccinia virus encoding bacteriophage T7 RNA polymerase for transient gene expression in mammalian cells. Virology. 1995;210(1):202-5.
82. Hallak Louay K, Spillmann D, Collins Peter L, Peeples Mark E. Glycosaminoglycan Sulfation Requirements for Respiratory Syncytial Virus Infection. Journal of Virology. 2000;74(22):10508-13.
83. Willemsen J, Neuhoff M-T, Hoyler T, Noir E, Tessier C, Sarret S, et al. TNF leads to mtDNA release and cGAS/STING-dependent interferon responses that support inflammatory arthritis. Cell Reports. 2021;37(6):109977.
84. Im K, Mareninov S, Diaz MFP, Yong WH. An Introduction to Performing Immunofluorescence Staining. Methods Mol Biol. 2019;1897:299-311.
85. Elliott AD. Confocal Microscopy: Principles and Modern Practices. Curr Protoc Cytom. 2020;92(1):e68.

86. Manders EMM, Verbeek FJ, Aten JA. Measurement of co-localization of objects in dual-colour confocal images. J Microsc. 1993;169(3):375-82.
87. Costes SV, Daelemans D, Cho EH, Dobbin Z, Pavlakis G, Lockett S. Automatic and quantitative measurement of protein-protein colocalization in live cells. Biophys J. 2004;86(6):3993-4003.
88. Kuo LJ, Yang LX. Gamma-H2AX - a novel biomarker for DNA double-strand breaks. In Vivo. 2008;22(3):305-9.
89. Deng Y, Yi X, Gong Y, Zhou L, Xie D, Wang J, et al. Palmitic acid induces nDNA release to cytosol and promotes microglial M1 polarization via cGAS-STING signaling pathway. Biochimica et Biophysica Acta (BBA) - Molecular Cell Research. 2023;1870(1):119385.
90. Mackenzie KJ, Carroll P, Martin C-A, Murina O, Fluteau A, Simpson DJ, et al. cGAS surveillance of micronuclei links genome instability to innate immunity. Nature. 2017;548(7668):461-5.
91. Rai KR, Shrestha P, Yang B, Chen Y, Liu S, Maarouf M, Chen JL. Acute Infection of Viral Pathogens and Their Innate Immune Escape. Front Microbiol. 2021;12:672026.
92. Orzalli MH, Broekema NM, Diner BA, Hancks DC, Elde NC, Cristea IM, Knipe DM. cGAS-mediated stabilization of IFI16 promotes innate signaling during herpes simplex virus infection. Proc Natl Acad Sci U S A. 2015;112(14):E1773-81.
93. Song JX, Villagomes D, Zhao H, Zhu M. cGAS in nucleus: The link between immune response and DNA damage repair. Front Immunol. 2022;13:1076784.
94. Kovacs MT, Vallette M, Wiertsema P, Dingli F, Loew D, Nader GPF, et al. DNA damage induces nuclear envelope rupture through ATR-mediated phosphorylation of lamin A/C. Mol Cell. 2023;83(20):3659-68.e10.
95. Buxboim A, Swift J, Irianto J, Spinler KR, Dingal PC, Athirasala A, et al. Matrix elasticity regulates lamin-A,C phosphorylation and turnover with feedback to actomyosin. Curr Biol. 2014;24(16):1909-17.
96. Bereiter-Hahn J, Jendrach M. Mitochondrial dynamics. Int Rev Cell Mol Biol. 2010;284:1-65.
97. Eze MO. Membrane fluidity, reactive oxygen species, and cell-mediated immunity: Implications in nutrition and disease. Medical Hypotheses. 1992;37(4):220-4.
98. Hu M, Bogoyevitch MA, Jans DA. Respiratory Syncytial Virus Matrix Protein Is Sufficient and Necessary to Remodel Host Mitochondria in Infection. Cells. 2023;12(9).
99. Liang Q, Seo Gil J, Choi Youn J, Kwak M-J, Ge J, Rodgers Mary A, et al. Crosstalk between the cGAS DNA Sensor and Beclin-1 Autophagy Protein Shapes Innate Antimicrobial Immune Responses. Cell Host & Microbe. 2014;15(2):228-38.
100. Yao M, Wu Y, Cao Y, Liu H, Ma N, Chai Y, et al. Autophagy-Mediated Clearance of Free Genomic DNA in the Cytoplasm Protects the Growth and Survival of Cancer Cells. Front Oncol. 2021;11:667920.
101. Chazotte B. Labeling nuclear DNA using DAPI. Cold Spring Harb Protoc. 2011;2011(1):pdb.prot5556.
102. Miyashita T. Confocal microscopy for intracellular co-localization of proteins. Methods Mol Biol. 2004;261:399-410.
103. Rothkamm K, Löbrich M. Evidence for a lack of DNA double-strand break repair in human cells exposed to very low x-ray doses. Proc Natl Acad Sci U S A. 2003;100(9):5057-62.

104. Kinner A, Wu W, Staudt C, Iliakis G. Gamma-H2AX in recognition and signaling of DNA double-strand breaks in the context of chromatin. Nucleic Acids Res. 2008;36(17):5678-94.
105. Rothkamm K, xf, brich M. Evidence for a Lack of DNA Double-Strand Break Repair in Human Cells Exposed to Very Low X-Ray Doses. Proceedings of the National Academy of Sciences of the United States of America. 2003;100(9):5057-62.
106. Davalli P, Mitic T, Caporali A, Lauriola A, D'Arca D. ROS, Cell Senescence, and Novel Molecular Mechanisms in Aging and Age-Related Diseases. Oxid Med Cell Longev. 2016;2016:3565127.
107. Simpson J, Spann KM, Phipps S. MLKL Regulates Rapid Cell Death-independent HMGB1 Release in RSV Infected Airway Epithelial Cells. Front Cell Dev Biol. 2022;10:890389.
108. Harker JA, Snelgrove RJ. A Not-So-Good Way to Die? Respiratory Syncytial Virus-induced Necroptotic Cell Death Promotes Inflammation and Type 2-mediated Pathology. Am J Respir Crit Care Med. 2020;201(11):1321-3.
109. Bedient L, Pokharel SM, Chiok KR, Mohanty I, Beach SS, Miura TA, Bose S. Lytic Cell Death Mechanisms in Human Respiratory Syncytial Virus-Infected Macrophages: Roles of Pyroptosis and Necroptosis. Viruses. 2020;12(9).
110. Senft AP, Taylor RH, Lei W, Campbell SA, Tipper JL, Martinez MJ, et al. Respiratory syncytial virus impairs macrophage IFN-alpha/beta- and IFN-gamma-stimulated transcription by distinct mechanisms. Am J Respir Cell Mol Biol. 2010;42(4):404-14.
111. Kalliara E, Kardynska M, Bagnall J, Spiller DG, Müller W, Ruckerl D, et al. Post-transcriptional regulatory feedback encodes JAK-STAT signal memory of interferon stimulation. Front Immunol. 2022;13:947213.

# Appendix

**Table A1**: Primary antibodies used in Western Blotting (WB) and immunofluorescence microscopy (IF).

| **Antibody** | **Manufacturer (Catalog number)** | **Dilution** | **Source/Isotype** |
|---|---|---|---|
| Calnexin | Cell Signaling Technology (#2679) | 1:1000 (WB) | Rabbit IgG |
| cGAS | Cell Signaling Technology (#15102) | 1:1000 (WB)<br>1:50 (IF) | Rabbit IgG |
| GAPDH | Cell Signaling Technology (#5174) | 1:10 000 (WB) | Rabbit IgG |
| H3 | Abcam (ab1719) | 1:1000 (WB) | Rabbit IgG |
| Lamin A/C | Cell Signaling Technology | 1:2000 (WB) | Mouse IgG2a |
| Lamin B1 | Abcam (ab16048) | 1:10 000 (WB) | Rabbit IgG |
| MRPL11 | Cell Signaling Technology (#2066) | 1:1000 (WB) | Rabbit IgG |
| Mouse IgG1 | MyBioSource (MBS679010) | 1:10 (IF) | Mouse IgG1 |
| Phospho TBK1/NAK (Ser172) | Cell Signaling Technology (#5483) | 1:1000 (WB) | Rabbit IgG |
| Phospho-IRF3 (Ser396) | Cell Signaling Technology (#4947) | 1:1000 (WB) | Rabbit IgG |
| Phospho-NF-kB p65 (Ser536) | Cell Signaling Technology (#3033) | 1:1000 (WB) | Rabbit IgG |
| Phospho-STAT1 (Tyr107) | Cell Signaling Technology (#9167) | 1:1000 (WB) | Rabbit IgG |
| Phospho-STING (Ser366) | Cell Signaling Technology (#50907) | 1:1000 (WB) | Rabbit IgG |
| Rabbit IgG Isotype control | Cell Signaling Technology (#3900) | 1:7350 (IF) | Rabbit IgG |
| RSV (2F7) | Novusbio (#NB110-37246) | 1:500 (WB) | Mouse IgG1 |
| STING | Cell Signaling Technology (#13647) | 1:2000 (WB) | Rabbit IgG |

| | | | |
|---|---|---|---|
| TGN38 | Santa Cruz (sc-166594) | 1:1000 (WB) | Mouse IgG1 |
| α-tubulin | Santa Cruz (sc-8035) | 1:200 (WB) | Mouse IgM |
| γH2AX (Ser139) | Sigma-Adrich (05-636) | 1:1000 (WB)<br>1:100 (IF) | Mouse IgG1 |

**Table A2**: Secondary antibodies used in Western Blotting (WB) and immunofluorescence microscopy (IF).

| **Antibody** | **Manufacturer (Catalog number)** | **Dilution** | **Immunogen** |
|---|---|---|---|
| IRDye GAR800CW | LI-COR Biosciences (#926-32211) | 1:5000 (WB) | Rabbit |
| IRDye GAR680RD | LI-COR Biosciences (#926-68071) | 1:20 000 (WB) | Rabbit |
| IRDye GAM800CW | LI-COR Biosciences (#926-32210) | 1:5000 (WB) | Mouse |
| Alexa Fluor™ 647 GAR IgG (H+L) | Thermo Fisher Scientific (A-21244) | 1:500 (IF) | Rabbit |
| Alexa Fluor™ 647 GAM IgG (H+L) | Thermo Fisher Scientific (A-21235) | 1:1000 (IF) | Mouse |
| Alexa Fluor™ 555 GAM IgG (H+L) | Thermo Fisher Scientific (A-21422) | 1:1000 (IF) | Mouse |

**Table A3**: Primer sequences used in qPCR.

| **Gene** | **Forward (5'-3')** | **Reverse (5'-3')** |
|---|---|---|
| *GAPDH gDNA* | TCCTCTGACTTCAACAGCGAC | AGAGTTGTCAGGGCCCTTTT |
| *MT-CO2* | AATCGAGTAGTACTCCCGATTG | TTCTAGGACGATGGGCATGAAA |
| *MT-ND1* | CACCCAAGAACAGGGTTTGT | TGGCCATGGGTATGTTGTTAA |
| *RNA 18S gDNA* | GTAACCCGTTGAACCCCATT | CCATCCAATCGGTAGTAGCG |

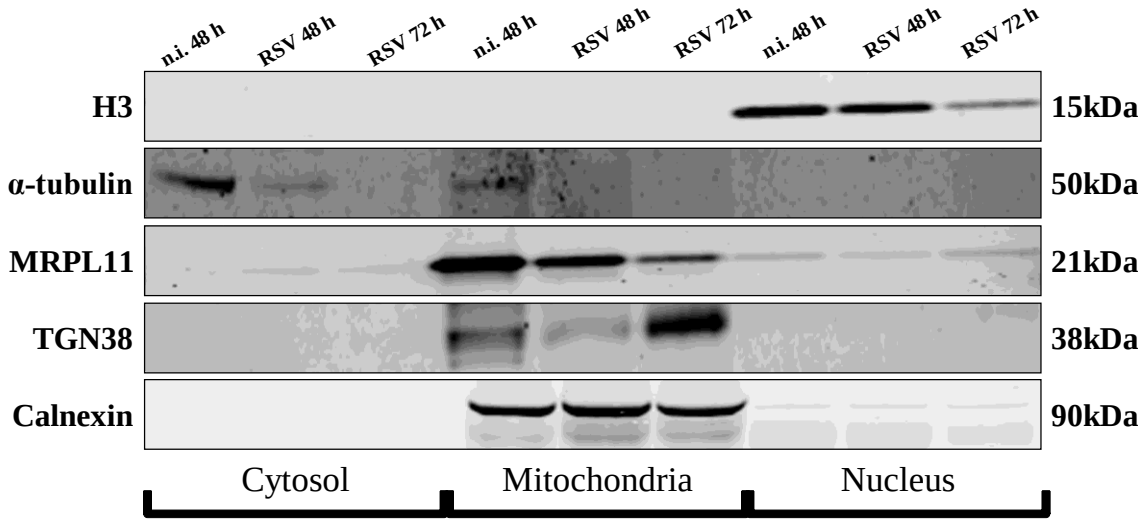


**Figure A1: Validation of fractionation experiments.** Wi-38 cells were infected with RSV for 48 h and 72 h. Subsequently, three cellular fractions were obtained: cytosol, mitochondria, and nucleus, each enriched for proteins characteristic of their respective compartments. Histone H3 was used as a nuclear marker, α-tubulin as a cytosolic marker, and MRPL11 as a mitochondrial marker. In addition, TGN38 as a Golgi marker and Calnexin as an endoplasmic reticulum marker were assessed and found to be present primarily in the mitochondrial fraction.

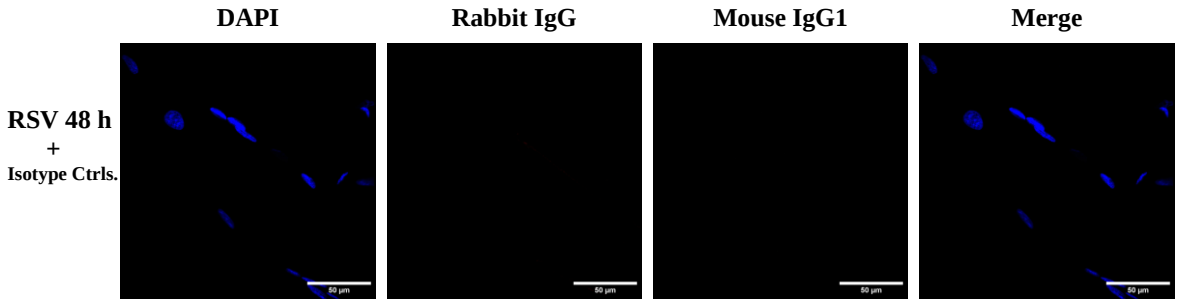


**Figure A2: Isotype controls for the co-localization experiment.** Cells were infected with RSV at a MOI of 3 for 48 h before fixation, staining, and microscopy analysis. These cells were stained with rabbit IgG and mouse IgG1 isotype controls, which serve as negative controls for cGAS and γH2AX respectively.

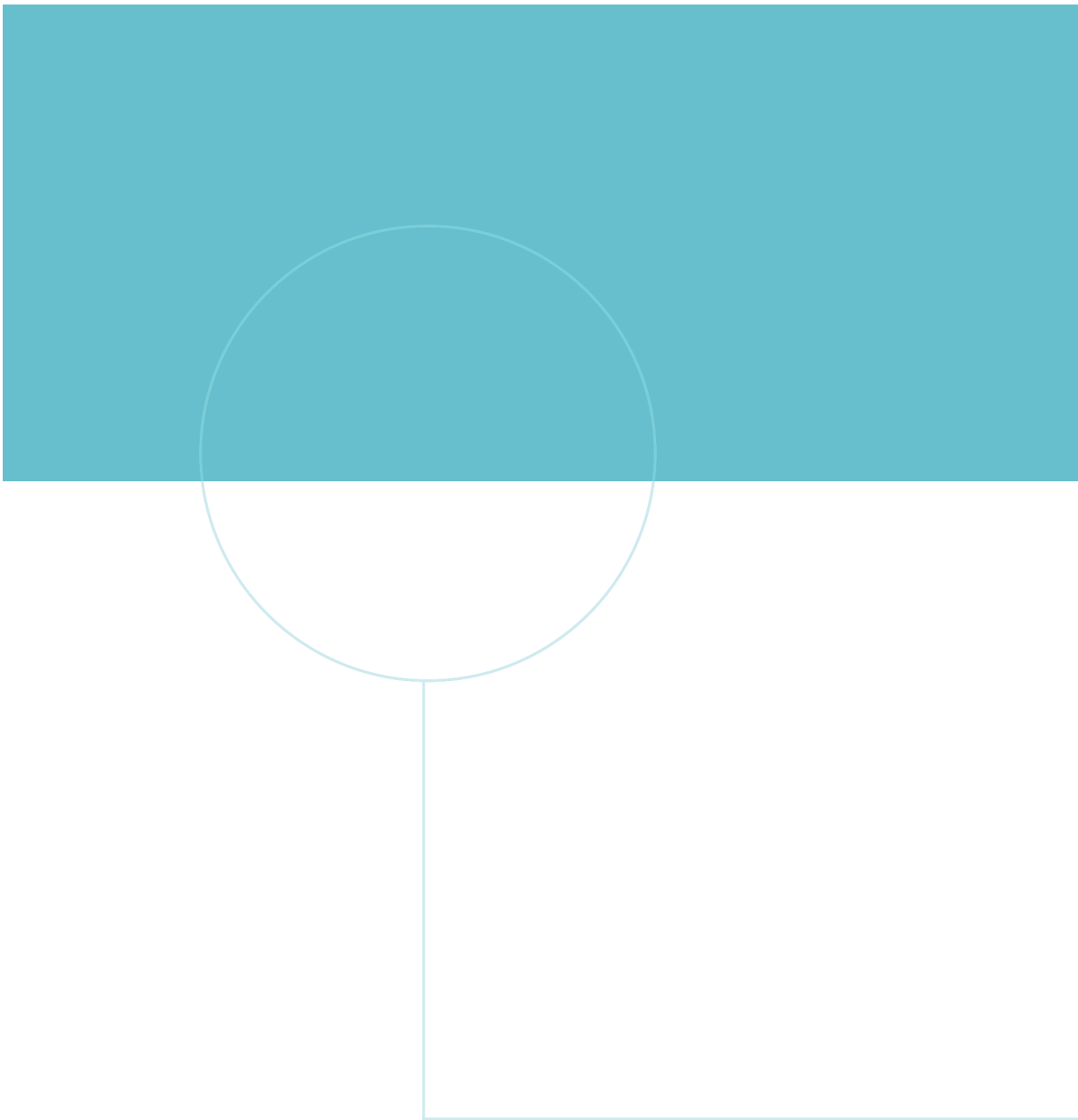

NTNU

Norwegian University of
Science and Technology